

Cesium atoms in cryogenic argon matrix

T. Battard⁽¹⁾, S. Lahs⁽¹⁾, C. Crépin⁽²⁾, and D. Comparat^{(1)*}

⁽¹⁾ *Université Paris-Saclay, CNRS, Laboratoire Aimé Cotton, 91405, Orsay, France.* and

⁽²⁾ *Université Paris-Saclay, CNRS, Institut des Sciences Moléculaires d'Orsay, 91405, Orsay, France*

(Dated: May 23, 2023)

We present an experimental and theoretical investigation of the spectroscopy of dilute cesium (Cs) atoms in a solid argon (Ar) matrix at cryogenic temperatures. The system considered is relevant for matrix isolation spectroscopy, and is at the basis of a recently proposed method for measuring phenomena beyond the standard model of particle physics. Absorption spectra are recorded at various deposition temperatures, and the evolution with temperature after deposition is also investigated. Using Cs-Ar and Ar-Ar pairwise interaction potentials, we perform a trapping site stability study that tends to favor two trapping sites of T_d (tetrahedral, 4 vacancies) and O_h (cubic, 6 vacancies) symmetries. By a mean-field analysis of the long-range Cs(6s,6p)-Ar-Ar triple dipole interaction added to a temperature-dependent zero point energy shift, we propose effective Cs(6s,6p)-Ar pairwise potentials. Using such pairwise potentials added with spin-orbit, we obtained reasonable agreement between observed and simulated absorption line positions. For a given trapping site, the triplet spectral shape cannot be reproduced using the semi-classical thermal Monte Carlo based on Mulliken type of differences between the excited and ground potential curves. However, we develop a simple first-order crystal field theory with only 6 interaction mode coordinates and, with quantized (phonon) normal modes and reflection approximation, we reproduce the triplet structure observed but unfortunately not the splitting. Further investigations are therefore needed, and we cannot affirm that the two structures we observed are due to T_d (tetrahedral, 4 vacancies) and O_h (cubic, 6 vacancies) symmetries

I. INTRODUCTION

Even though matrix isolation spectroscopy has been studied since the 1950s [1–3], the shape and behavior of the trapping environments inside the matrix remain barely understood. Even for the most simple systems containing single valence electron atoms (alkali atoms) inside rare gas matrix environments, there is no consensus yet on the trapping site with the host atom (especially for heavy atoms) [4–6]. A more precise understanding of the trapping site and of the matrix effect on the dopant, would be important for precise spectroscopy experiments like magnetometry, other spin-dependent interactions, or for investigating new physics beyond the Standard Model, such as searches for fundamental (parity, time-reversal) symmetries violations as electric dipole moment (EDM) particles, or axion-like dark-matter candidates [7–13].

In this article, we study cesium atoms trapped in an argon matrix. Understanding this simple system should also help to characterize more complex experiments. Among the (stable) alkali atoms, Cs is the heaviest one, making it most sensitive to the effects of the electron EDM [14]. Argon has been chosen because being the only isotopically pure rare gas without any nuclear spin that could interact with the cesium spin. Absorption (or transmission) spectra are the basis of all optical manipulations required for the above proposed experiments. However, interestingly enough, to our knowledge, only

few experiments studied Cs embedded in Argon [15, 16] and only two optical transmission spectra have been published [17, 18] ([19] gives only bands absorption and emission frequencies). For Cs in Ar, two structures were observed and attributed to $6s \rightarrow 6p$ transition in two different trapping site environments: the $6p$ triplet degeneracy being lifted by a dynamical Jahn-Teller effect. An interpretation with two different trapping sites (of cubic symmetry) was given in Ref. [17, 18] (experiment performed at 1.8 K on glass and Sapphire window) but Ref. [19] observed, in addition, $6s \rightarrow 5d$ and $6s \rightarrow 7p$ transitions together with relaxation and fluorescence from $6p$ and $5d$ level (experiment performed at 10 K). In this article, we perform new experiments in order to solve the discrepancies between previous measurements. Below, we first present the experimental setup, allowing precise Cs density measurement in the highly polycrystalline Ar samples. Then, using Cs-Ar and Ar-Ar pairwise interaction potentials, we first perform a trapping site stability study. By correcting the pairwise interaction by effective third-order effects, we predict absorption line positions for the different trapping sites found. We finally check, thanks to a simple crystal field model, if the linewidth found is compatible with the proposed trapping sites. We then conclude on possible improvements needed to go further.

II. EXPERIMENTAL SETUP

Figure 1 shows the experimental setup. To grow the cryogenic matrix, Ar gas is deposited onto a 20 mm diameter, 1 mm thick C-cut sapphire (Al_2O_3) plate embedded in a copper frame. The plate is mounted in a

* Corresponding author: daniel.comparat@universite-paris-saclay.fr

cryostat (by the company Mycryofirm) with vibration decoupling in a chamber in high vacuum conditions of $\sim 1 \times 10^{-7}$ mbar. It is powered by a pulsed tube cryocooler (SHI RP082B2S). The range of cryogenic temperatures, between 3 K and 30 K, for the sample holder is achieved by resistive heating. To reduce thermal perturbation by transfer of the Ar beam's kinetic energy, the temperature of the sample holder is maintained constant by a PID loop.

A. Ar crystal growth

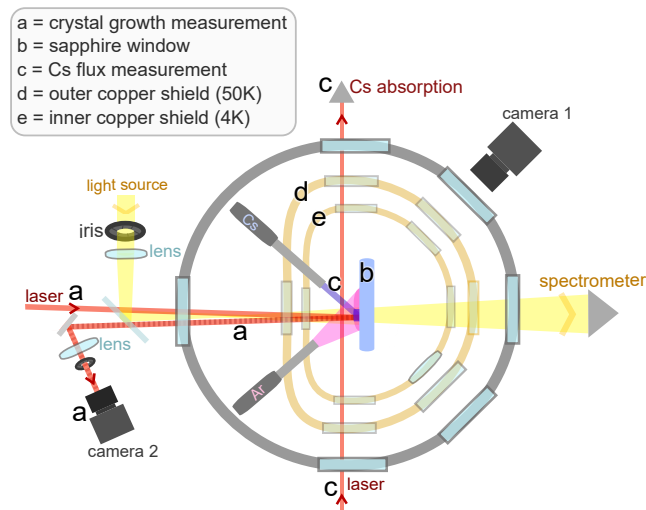


FIG. 1. (Color available online) Schematics of the cryostat and of the optical systems used for monitoring the matrix growth rate and measuring the absorption and fluorescence spectra. The arrows indicate the propagation directions of the beams. The laser illumination of the matrix growth interface is imaged on CCD camera 2 to display the interference pattern.

The thickness L of the argon layer is monitored in real time, mainly by 2D reflection Fizeau interferometry. The pattern formed by interferences between the reflected light from the front and back sides of the matrix is imaged by a lens onto a CCD camera. The 2D imaging has many advantages compared to previous 1D transmission or reflection laser interferometry studies [20–22]: it is background-free, so it has very good contrast. It is much less limited by beam size and spatial interference narrowing, and it allows to monitor the whole sample and ensures its overall quality during deposition.

For this Ar growth measurement, a DFB diode laser at $\lambda = 852$ nm was chosen. It has the advantage that it can also be used to monitor the Cs flux by saturated absorption.

The interference fringes of a given point evolve as $\frac{2n_{\text{Ar}}}{\lambda} \frac{dL}{dt}$ with $n_{\text{Ar}} = 1.3$ the refraction index of an argon bulk crystal at 852 nm [23].

We observe a growth of ~ 3 fringes per minute corresponding to a growth rate for an ideal argon bulk crystal of $\frac{dL}{dt} = 1 \mu\text{m}/\text{min}$. We typically deposit Ar for around one hour, resulting in a crystal with a thickness in the range of 50 μm .

B. Cs density

In order to insert cesium into the matrix, we use Alfavakuo e.U. Alfasource 3S dispensers with a CsBi₂₅ alloy. The alkali purity is 99,980% for cesium. The dispenser is mounted outside the 50 K and 4 K thermal shields and activated by resistive current heating. The Cs vapor is directed to the substrate by a $d = 4$ mm inner diameter steel tube that passes through both thermal screens. The tube is independently heated to $\sim 40^\circ\text{C}$ with resistors to reduce clogging. We have studied in detail in Ref. [24] the behavior of effusion of cesium atoms through a collimating tube and found that whatever the tube material is, the Cs sticks on the wall. This produces a very well-collimated homogeneous Cs atomic beam.

In order to monitor the Cs flux, we record a laser absorption spectrum when scanning the frequency of the low-intensity diode laser crossing the cesium beam. We assume that the Cs beam diameter coincides with the inner tube diameter d and that its density n is uniform. This is confirmed by scanning the laser beam through the atomic beam or by a simple 2D absorption image of the Cs in the Ar matrix where the cesium-doped zone forms an apparent spot about 5 mm wide. The velocity distribution is effusive [24]:

$$f_z(v_z) = \left(\frac{m}{\sqrt{2k_B T_z}} \right)^2 v_z^3 e^{-\frac{mv_z^2}{2k_B T_z}}$$

along z . The Cs beam is intersected by the laser at an angle of $\alpha = 22^\circ$ in regard to the beam axis, as shown in Fig. 1. Therefore the (Beer-Lambert-Bouguer) absorption is given by $nd\sigma_0 \int_0^\infty \frac{1}{1 + \left(\frac{\omega_L - \omega_{\text{Cs}} - kv_z \sin \alpha}{\Gamma/2} \right)^2} f_z(v_z) dv_z$

where $\sigma_0 = 1.413 \times 10^{-9} \text{cm}^{-1}$ is the absorption cross section for an isotropic light polarization at the resonant $6s_{1/2}(F = 4) \rightarrow 6p_{3/2}(F = 5)$ frequency $\hbar\omega_{\text{Cs}}$ with a natural spontaneous decay rate of $\Gamma = 1/(30.4 \text{ns})$ [25]. We simply fit the experimental absorption profile while scanning the laser (angular) frequency ω_L to this formula. Results are compatible with, and not very sensitive to, $T_z \approx 400$ K. We then found the beam density n and so the Cs flux $n\pi(d/2)^2 \bar{v}$ where $\bar{v} = \sqrt{8k_B T_z / \pi m}$ is the average velocity. We record only population in the hyperfine level $F = 4$ (that is only 9/16 of the overall Cs(6s) population in the beam assuming Boltzmann-equidistribution between the 9 times degenerate $F = 4$ and 7 times $F = 3$ levels). Finally, we end up with a Cs(6s) flux of few 10^{12} at/s arriving on the Ar matrix. We thus expect a $\sim 10^{-3}$ atomic ratio of Cs in the argon matrix (density on the order of 10^{18}cm^{-3}) and a typical average internuclear distance between Cs atoms on the order of 10 nm.

To avoid Cs pollution of the window and to produce

well-defined trapping environments for all the Cs atoms, we always start the Cs deposition only after a few micrometers of Ar are already deposited.

C. Quality of the samples

Clearly, an fcc Ar crystal cannot be grown on the hexagonal lattice of sapphire [26]. No epitaxy is possible, and we expect several crystal defects with holes or cavities formation, such as observed in Ref [26].

Cs can, in principle, be trapped either in point defects surrounded by vacancies but also in line-dislocations defects (screw, edge, ...), on surface defects (stacking fault, tilt and twist grain boundaries), or even in volume defects (pores, cracks, another phase like hcp inclusions, ...) [27].

Literature shows that grain size is inversely proportional to the growth rate [28] and that the deposition temperature plays a major role in the crystal quality. Indeed, crystals contain twins, stacking faults, and dislocations [29]. There is roughly 8 nm distance between dislocations at 20 K and 3 nm at 10 K [30, 31] so we probably have small crystallites on the order of thousands of atoms separated by dislocations. Similarly, it was found that film grown at a condensation temperature greater than 2/3 of the sublimation one (that is 30 K for Ar), the fcc grains have about 100 nm size whereas at 1/3 of the sublimation temperature (so at 10 K for Ar) the grain size is of about 10 nm with evidence for minority hcp phase [28, 32, 33]. Moreover, below a critical temperature (18 K for Ar), some atomic-scale cavities become present in the lattice [34].

These studies seem consistent with what we observed in our experiment regarding the quality of the Fizeau interference image during crystal growth and the intensity loss in light transmission due to scattering off grain boundaries. Indeed, a sample becomes almost opaque when the Ar crystal grain diameter is of the order of 0.1λ due to light scattering from the grain boundaries [35].

We have tried to perform annealing up to 30 K. But no drastic modification occurs in the Ar crystal quality. This is indeed expected because higher temperatures (closer to the triple point) would be needed [36, 37] to favor vacancies formation or atom-vacancy exchange by diffusion [38–40] which is impossible to reach in a free-standing sample in vacuum because sublimation arises sooner due to the high vapor pressure of solid argon.

III. ABSORPTION SPECTRA

A. Experimental spectra

For the absorption (or transmission) spectroscopy, an Avantes AvaLight-HAL tungsten-halogen light source, together with an ocean optics QE65000 spectrometer, is

used. The spectrometer was calibrated by measuring the spectra of Hg and Kr lamps.

To measure the absorption in the doped Ar crystal, the light from the lamp is directed through the sample. Its position and shape on the plate can be controlled with irises and mirrors and monitored by a camera.

We then record the spectral absorbance of the sample due to the Cs $A = \log_{10} \frac{I_0}{I_t}$ where I_t is the spectral irradiance density recorded in presence of the Cs-Ar sample and I_0 taken before any Cs was deposited.

The recorded spectra from different deposition temperatures are presented in Fig. 2 a). Above 14 K, the spectra become very broad, and we had difficulties producing any spectra above this temperature.

On the contrary, if Cs and Ar are deposited at low temperature, 8 K in the example of Fig. 2 b), the spectra remain visible even if the sample is further heated up to ~ 35 K temperature above which the argon starts to sublimate under vacuum.

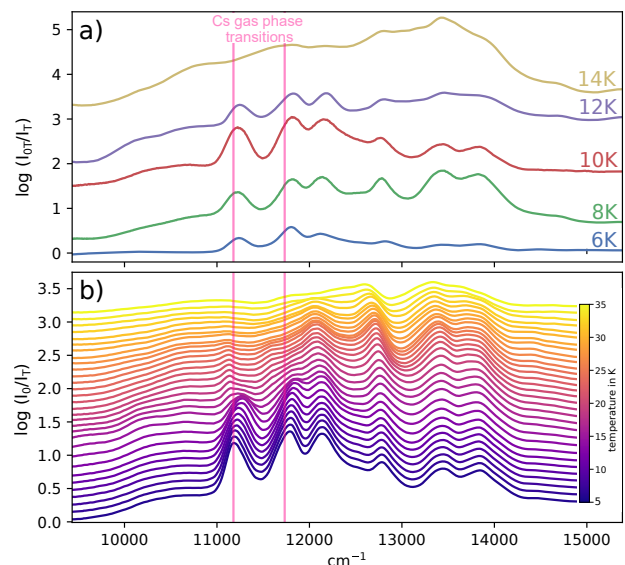


FIG. 2. a) Absorbance spectra of Cs embedded in Ar for deposits performed at different temperatures. b) Evolution with temperature for a spectrum initially created at 8 K. The spectra are offset in ordinate from one another for better visual clarity. For reference, the positions of the $6s_{1/2} \rightarrow 6p_{1/2}$ (left) and $6s_{1/2} \rightarrow 6p_{3/2}$ (right) Cs gas-phase transitions are indicated.

The spectra clearly show two triplet structures similar to the ones observed by [17, 18], assigned to two kinds of trapping sites. The different relative intensities of the two triplets in the various samples (Fig. 2 a)) suggests that depending on the deposition conditions (depositing rate, sample density, temperature, argon purity, ...), one or the other trapping site gets favored. It is important to note that we chose slightly different Ar and Cs fluxes for different samples. The numbers given in the previous section were typical values that can be easily modified by a factor of 3 between different experiments. The

temperature evolution shown in Fig. 2 b) shows a more significant spectral deformation in the red site (between 11 000 and 12 500 cm^{-1}) than in the blue site (between 12 500 and 14 000 cm^{-1}). The temperature changes below 20K are mainly reversible. They consist of a slight spectral shift of the bands (red or blue shift, depending on the band) and a slight band broadening. Heating beyond 20K usually leads to a drop in the baseline (probably due to stronger scattering of the light in the Ar), together with irreversible changes in the red triplet. The blue site, however, remains well-defined until 28K.

More generally, these types of triplet structures are well-known in alkali atoms trapped in rare gas matrices : They are not due to resolved phonon lines but are created by homogeneous broadening and are due to the lifting of degeneracy of the p level by the crystal environment [4]. However, due to the finite temperature, it is not easy to distinguish between the splitting created by a low symmetry crystalline field, such as in dislocations or surface defects, and one created by a (temperature-dependent) dynamical Jahn-Teller effect in a more symmetric (cubic, tetrahedral, ...) crystalline field. From the shape of the lines, it seems, however, already clear that the main splitting is on the order of the fine structure splitting between $6p_{1/2}$ and $6p_{3/2}$ (of nearly 554 cm^{-1} in gas phase). Then the static or dynamical electric crystal field will lift the degeneracy between the $|m| = 3/2$ and $|m| = 1/2$ of the $6p_{3/2}$ level.

B. Trapping sites

1. Potential curves

In order to study the possible trapping sites in an fcc lattice, we should perform a stability study.

If using a Lennard-Jones potential with the same depth $\sim 45 \text{ cm}^{-1}$ and equilibrium distance $\sim 0.55 \text{ nm}$ than the $X^2\Sigma_{1/2}^+$ Cs-Ar potential [41–43], a generic accommodations of an atom in fcc and hcp rare-gas solids calculation [6, 44] indicates that possible trapping sites for Cs in an Ar fcc matrix are likely to be with 6, 8, or maybe 10 vacancies and of respectively O_h , C_{2v} , C_{4v} symmetry. However a 7-vacancy fcc lattice (C_{3v} symmetry) or a 5-vacancy trapping site located in an hcp environment or a grain boundary similar to a stacking fault accommodation (D_{3h} symmetry) may also appear [5, 45].

However, as shown in Fig. 3 c) Lennard-Jones potential badly reproduces the Cs-Ar ground state interaction. We thus performed our own study using more accurate potentials.

For the $V_{\text{Ar-Ar}}$ potentials, we use the simple analytical formula given by [46]. For the Cs-Ar ground state $V_{\text{Ar-Cs}} = V_{X^2\Sigma_{1/2}^+}$ we use the potential curve from Ref. [42] with a third order interpolation between points and, due to the lack of points in the long-range, we use parts of

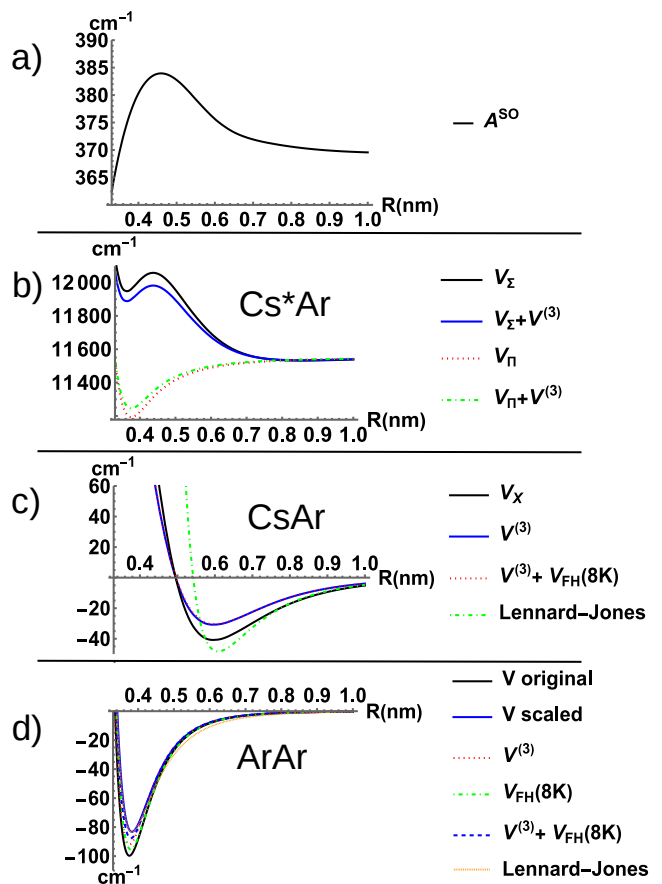


FIG. 3. a) Spin-orbit constant for Cs(6p)-Ar interaction. b) Cs(6p)-Ar potential curves. c) Cs(6s)-Ar potential curves. d) Ar-Ar ground state potential curves. The potential curves V used in this work are also compared to the one with zero point energy V_{FH} , and a third order $V^{(3)}$ correction. The original potentials being the [42] ones. For the excited state, we have chosen to plot only a third-order case with no cut-off (in a pure analogy with the ground state case, see text); that is the two body potential V (offset by $E(6p)$) multiplied by $\frac{1}{3} \frac{8\pi\rho}{9} \frac{C_6^*}{C_6}$.

the potential from [41] for inter-nuclear distances above 2 nm. The potentials are shown in Fig. 3. Though the Lennard-Jones approximation is very good for the Ar-Ar potential, it is quite off for the Cs-Ar one.

For the full Ar-Ar and Cs-Ar interactions, we use a simple two-body (pairwise potential) approximation where the full interaction energy of a Cs doped crystal with $(N-n)$ Ar atoms and n vacancies, is given, with obvious notations, by

$$V = \sum_{i=1}^{N-n} V_{\text{Ar-Cs}}(\mathbf{R}_{\text{Cs-Ar}_i}) + \sum_{1 \leq i < j \leq N-n} V_{\text{Ar-Ar}}(\mathbf{R}_{ij}) \quad (1)$$

We start by using a simple cubic grid with $N = 4 \times 7^3 = 1372$ atoms (the factor 4 comes from the 4 atoms in the fcc primitive cell). Convergence is already obtained to

the percent of the energy for this configuration, and this number of atoms allows us to simulate a small piece of crystal between two dislocations.

For a central Ar atom at location \mathbf{R}_0 , the sum over all other atoms $\sum_i V_{\text{Ar-Ar}}(\mathbf{R}_0 - \mathbf{R}_i)$ reaches $\approx 773 \text{ cm}^{-1}$ (here a slightly larger grid is required to reach convergence) that significantly overestimate the experimental value for the cohesive energy of 645 cm^{-1} [47, 48]. Similarly, the equilibrium distance is found for a lattice constant of 0.521 nm , compared to the correct value 0.531 nm [48]. In order to reproduce the correct cohesive (also called atomization $-E_{\text{at}}$) energy and the equilibrium lattice constant, we scale the Ar-Ar potential by $V = \alpha V_{\text{Ar-Ar}}(\beta R)$ with $\alpha = 645/773$ and $\beta = 0.521/0.531$. Other choices of empirically modified potentials, such as $\alpha V_{\text{Ar-Ar}}(\beta + R)$ used in Ref. [49], lead to similar results. This is a simple way to keep the simple two-body pairwise picture but having the proper cohesive energy and the equilibrium lattice constant by including in an effective way many-body corrections and zero-point energy [48].

2. Site stability

To assess the thermodynamical stability of a n vacancy structure, we calculate a type of (Gibbs or Enthalpy, free) accommodation energy of the structure [44, 50, 51]: $\Delta E_N(n) = E_{\text{Cs}}(n, N) - E_{\text{Ar}}(N)(N - n)/N$, where $E_{\text{Cs}}(n, N)$ is the total energy of the system formed by a Cs atom embedded in the crystal and $E_{\text{Ar}}(N)$ is the total energy of the pure Ar crystal of N atoms without the vacancies. A condition for the system to be stable is that the dissociation of M systems with n vacancies in M' subsystems with n' vacancies and M'' subsystems with n'' vacancies is energetically not favorable. This requires $M\Delta E_N(n) < M'\Delta E_N(n') + M''\Delta E_N(n'')$ with $n''M'' + n'M' = nM$ (the number of atoms is conserved). For instance, two 5 vacancy systems can relax in the more stable, one 4 vacancy and one 6 vacancy situation. This means, for n vacancies to produce a stable trapping site, that $\Delta E_N(n)$ should belong to the convex hull of the free energy curve as a function of the number of vacancies [51, 52]. Clearly, other criteria, such as dynamical ones (migration and activation energies), are also crucial to understand the trapping sites. But the use of $\Delta E_N(n)$ is a crucial component. The $\Delta E_N(n)$ formula is useful for a small crystal, or in our case, for a small single crystallite in a poly-crystal, but also often used is the thermodynamical limit of $N \rightarrow \infty$ so with $E_{\text{Ar}}(N)/N \approx E_{\text{at}}$ and $\Delta E_N^\infty(n) = E_{\text{Cs}}(n, N) - E_{\text{Ar}}(N) + nE_{\text{at}}$ [53–57].

Obviously, only the most stable (minimal energy) configuration at fixed n value will be important. So, we do not span the whole position space for the Cs atom and for the vacancies, but we only start with the already predicted defects structures in fcc crystals [50, 53–63]. However, as it will also be needed for further study as the Jahn-Teller dynamical effect, we allow the Cs atoms and

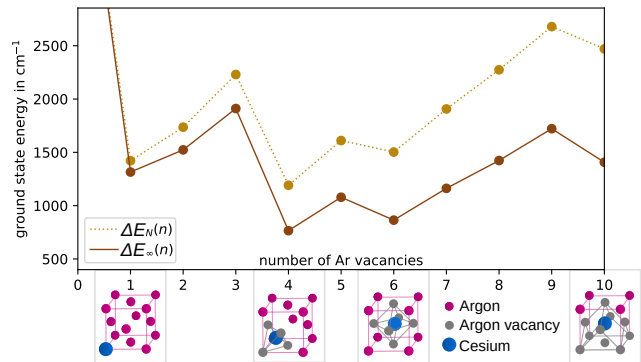


FIG. 4. Optimized configuration found to lower $\Delta E(n)$ for a given vacancy number n (for $N = 1372$ atoms). Both $\Delta E(n)$ and $\Delta E^\infty(n)$ are shown together with a picture of the final structure obtained for the Cs atom and some of the nearest neighbor Ar atoms.

the first 3 or 4 few (typically ~ 60) nearest neighboring Ar atoms layers to move and optimize their position to lower $\Delta E_N(n)$ as much as possible. We use one of "the best overall choice" (quoting [64, 65]) among gradient descent optimization algorithms, namely the Adaptive Moment Estimation (Adam) [66] and its modified version Nesterov-accelerated Adaptive Moment Estimation (Nadam) [67]. A faster way, when close to the optimum, is to use also the second order derivative (see discussion following Eq. (C1)) to correct for the equilibrium position of the normal coordinates [68]. We thus repeat the procedure and optimized the positions until a minimum is reached. Results are shown in Figure 4 for such optimized geometry. However, we mention that using initial fixed (pure) fcc Ar and vacancies positions is actually sufficient to reproduce the results well enough to predict the stable sites without any need for optimization of the atomic positions.

The result of this study differs from the one discussed previously and performed using a Lennard-Jones potential [6, 44] because it indicates that the most stable trapping sites are likely to be the T_d one with 4 vacancies and O_h with 6 vacancies. This seems consistent with our observation of two triplet lines in absorption.

C. Simulation of the position of the absorption lines

1. Line positions in the pairwise approach

Unlike the observation of Ref. [19] our data shown in Fig. 2 does not show evidence for Cs($6s \rightarrow 5d$) transition. Only Cs($6s \rightarrow 6p$) triplet structures seem visible, with almost no evidence of any other Cs levels involved nor of Cs dimers at the low density and temperature we work. Thus we are confident that a simple pairwise approximation diatomic in molecule (DIM) type of approach,

using only the Ar ground state and Cs(6s), Cs(6p) levels, should give good results to simulate the Cs(6s \rightarrow 6p) absorption spectra.

The calculation is detailed in appendix B. Briefly, the Cs(6s) energy shift is calculated as done previously for the stability study. Now, we add the 6p

manifold, where the energies are the eigenvalues of the Hamiltonian calculated by summing the interaction $\langle L'M'|\hat{V}_{Cs,Ar}(\mathbf{R}_{Cs,Ar} = \{X, Y, Z\})|LM\rangle$ between a Cs atom (with $|6pM\rangle$ levels quantized along an arbitrary but fixed axis z) with each Ar atom given by the matrix calculated using Wigner rotations:

$$\frac{1}{3}(2V_{\Pi}(R) + V_{\Sigma}(R))\mathbf{I}_3 + \frac{1}{6}\frac{V_{\Sigma}(R) - V_{\Pi}(R)}{R^2} \begin{pmatrix} |M = -1\rangle & |M = 0\rangle & |M = 1\rangle \\ X^2 + Y^2 - 2Z^2 & 3\sqrt{2}(X + iY)Z & -3(X + iY)^2 \\ 3\sqrt{2}(X - iY)Z & -2(X^2 + Y^2 - 2Z^2) & -3\sqrt{2}(X + iY)Z \\ -3(X - iY)^2 & -3\sqrt{2}(X - iY)Z & X^2 + Y^2 - 2Z^2 \end{pmatrix} \quad (2)$$

with also the spin-orbit $A^{\text{SO}}(R_{Cs,Ar})\mathbf{L}\cdot\mathbf{S}$ term added, where $R = \sqrt{X^2 + Y^2 + Z^2}$.

The $V_{\Pi}(R)$, $V_{\Sigma}(R)$ Hund's case (a) potential curves and the spin-orbit coefficient $A^{\text{SO}}(R)$, where R is the Cs-Ar separation, shown in Fig. 3, have been constructed from the most recent $V_{X^2\Sigma_{1/2}^+}$, $V_{A\Pi_{1/2}}$, $V_{A\Pi_{3/2}}$, $V_{B^2\Sigma_{1/2}^+}$ potentials [42] with the long-range part taken from the potentials of Ref. [41] that presents more points (but is calculated from a smaller basis set and is therefore less accurate at short range).

Because the variation of the spin-orbit coefficient $A^{\text{SO}}(R)$ is significant only for R smaller than the closest neighbors [69] (see Fig. 3 a), the use of a constant spin-orbit coefficient A^{SO} has only a very limited effect (we found at most a 10 cm^{-1} shift difference in the final Cs(6s)-Cs(6p) transition lines). Therefore in the following, we simply use the V_{Π} , V_{Σ} potentials curves and a constant spin-orbit coefficient A^{SO} .

Results for the Cs(6s)-Cs(6p) transition lines positions are shown in Fig. 5 (big dots). Obviously, in this 0K theoretical calculation, only doublets arise, not triplets, as expected in highly symmetric trapping sites, because of the absence of any thermal or dynamical broadening. However, there is reasonable agreement between the experimental and calculated positions.

It might be at first sight quite surprising that the most shifted lines, compared to the gas phase case, are the ones with 6 vacancies, whereas the more constrained 4 vacancies structure seems almost not affected. This fact that the red triplet is T_d and the blue one is O_h , is opposite to what is observed (or simulated) for other systems such as Na in Ar [70, 71]. This can be qualitatively explained by assuming a simplified model of Cs surrounded by Ar atoms in a symmetric spherical environment (a situation that indeed arises in solid He [72] with Cs enclosed in a He bubble). In such a spherical environment, the averaged interaction term is $2V_{\Pi} + V_{\Sigma}$ (see matrix (2)). Thus a good figure of merit to study the shift of the 6s - 6p line position is to look at $2V_{\Pi} + V_{\Sigma} - V_X$ which is shown in Fig. 6 with also the nearest neighbor positions in both the T_d and the O_h structures found in the stability study.

Fig. 6 indicates that the blue shift due to positive

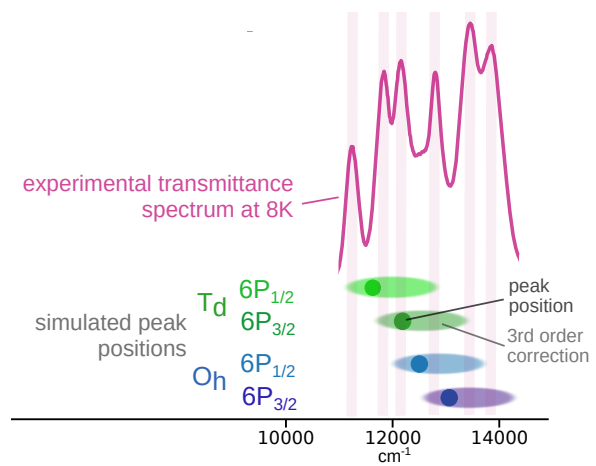


FIG. 5. Comparison between experimental transmittance spectra (solid blue line, same as in Fig. 2) and different theoretical models for the two trapping sites O_h with 6 vacancies and T_d with 4 vacancies. Bottom part: position of the 0K lines using pairwise potential: dots are the two body cases with potentials from [42]. The zero point energy barely shifts those lines (at most 150 cm^{-1}), but the estimation of the third-order effect (see text) produced an additional shift that we estimate to be within the elliptical areas.

$\Delta V = 2V_{\Pi} + V_{\Sigma} - V_X$ values is more pronounced for the O_h case than for the T_d one. This is mainly due to the fact that, in the O_h case, the first 8 and second 24 nearest neighbors (solvation type) shell creates per atom a $\sim 100\text{ cm}^{-1}$ blue shift, where, in the T_d case, the first shell almost produced no shift due to cancellation of $2V_{\Pi} + V_{\Sigma}$ and V_X shifts and the second shell is only composed of 12 atoms. Together with the red shifts created by longer range shells, this qualitatively explains the $\sim 2000\text{ cm}^{-1}$ blue shift in the O_h case and that cancellation leads to T_d lines appearing at almost the gas phase location.

As done for Ar-Ar potentials, to improve the comparison of the line positions, we have to add the zero-point energy and the Third-Order Many-Body interaction. Since these are only corrections, we did not use them to re-optimize the atomic positions.

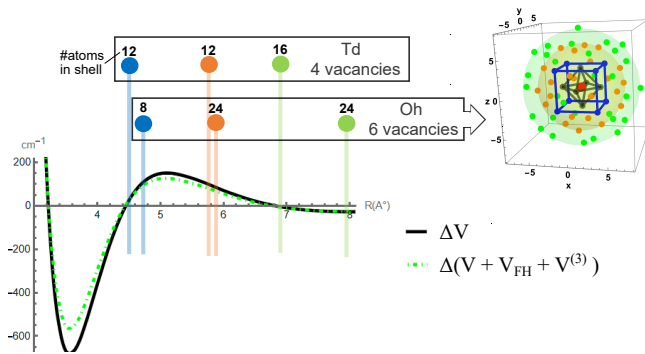


FIG. 6. $\Delta V = 2V_{\Pi} + V_{\Sigma} - V_X$ Cs-Ar potentials with offset of the asymptotic values with the first R_1 , second R_2 , and third R_3 nearest neighbor shells in the T_d and O_h cases (for O_h an example of the Cs and Ar positions is shown).

2. Third order (dipole-dipole-dipole type) correction

To our knowledge, the third-order correction has not been used previously for such simulated absorption spectra [4, 71]. However, its effect is not negligible for ground and even more for excited states.

We do not have any accurate three-body Cs-Ar-Ar potential curves, so we tried to approximate their contribution [73, 74]. As discussed in the appendix E, we use two and three-body expressions for the pure long dipolar range part in order to extrapolate a proper three-body potential valid also for shorter distances. We then sum it over all atoms. Unfortunately, the nearest neighbors play a major role [71], and this is where our formula is the least accurate. Therefore, we choose an even simpler approximation, similar to the Mutô-Stenschke-Marcelli-Wang-Sadus one [74–76], and we average the formula, in the mean-field sense for the position of the third Ar atom, in order to produce an effective correction to the two-body Cs-Ar potential. These are simple density-dependent expressions that relate the averaged three-body interactions to the two-body ones. This allows us to merge both kinds of interactions into effective Cs-Ar two-body potential curves. With this procedure, the final Cs-Ar potential curve is the original one corrected by the effective three-body one $\bar{E}_{12}^{(3)}$, leading finally to an effective two-body potential given by Eqs. (E9) and (E11).

Qualitatively the effect of this modification can be estimated from Eq. (E8), and using $2V_{\Pi} + V_{\Sigma} - V_X$ as a figure of merit for the shift. We see that the third order effect $\bar{E}_{12}^{(3)}$ has a $\frac{8\pi\rho}{3R^6}(C_9^* - C_9) > 0$ dependence, that thus should probably produce a net blue shift, where ρ is the Ar density and C_9, C_9^* are respectively the triple dipole coefficient for the ground and excited states. This can also be understood by looking at the potential curves given in Fig. 3. In this figure, the plotted third-order excited state potential curve is calculated in analogy with the ground state case so $V_{\Sigma}^{(3)} = (V_{\Sigma} - E(6p))\frac{1}{3}\frac{8\pi\rho}{9}\frac{C_9^*}{C_9^*}$ and $V_{\Pi}^{(3)} = (V_{\Pi} - E(6p))\frac{1}{3}\frac{8\pi\rho}{9}\frac{C_9^*}{C_9^*}$.

3. Correction for zero point energy correction

To consider the quantum effects due to the zero-point energy, we use the Feynman-Hibbs (equivalent to the Wigner-Kirkwood approach) temperature dependent effective correction to a pair potential between ground state atoms: $\Delta V_{FH}(R) = \sigma_0^2(V''(R) + 2V'(R)/R)$ where μ is the reduced mass and $\sigma_0 = \sqrt{\frac{\hbar^2}{24\mu k_B T}}$ is the Gaussian width of quantum particles given by the uncertainty principle [77, 78].

4. Absorption line positions

When adding the zero point energy and third order correction, we find new line positions for the absorption spectra shown in Fig. 5. In this calculation, for the excited states, we used the effective two-body potential (two-body corrected with three-body), and for the ground state, we further added the zero point energy using the Feynman-Hibbs $\Delta V_{FH}(R)$ correction with a temperature chosen to be the experimental one of 8K. We do not use this procedure for the Ar-Ar interaction because we already have a well-scaled potential, but it is interesting to validate this procedure on the known Ar-Ar case. Figure 3 indicates that this approach of correcting a two-body potential by $\Delta V_{FH}(R) + \bar{E}^{(3)}$ reproduces quite well the scaled potential we used.

One of the main insights is that the zero-point energy is quite negligible (on the order of 100 cm^{-1}). The third-order correction, however, plays an important role and should not be neglected. It certainly deserves much more study. Indeed, we found that the shift created by the third-order effect is very sensitive to the chosen cut-off parameters and can even be attractive or repulsive, depending on their values. So the added shift has to be taken more as an indication of the effect created than a very quantitative result. This is the reason why we choose to put its effect as an uncertainty in our result. The ellipses in Fig. 5 playing the role of effective error bars have been roughly evaluated using different cut-off values (see Appendix E) and exponents in the power of the cut-off function, and using $V_{\Sigma}^{(3)}$ and $V_{\Pi}^{(3)}$ potential curves given in Fig. 3.

Within the large uncertainty of the 3rd order we are able to find qualitative agreement between theoretical line positions and experimental ones such as the fact that the O_h lines are on the blue side compared to the T_d one. But, we are not able to find the correct line separation between O_h and T_d . Using theoretical potential curves from Ref. [41] produced similar results, but blue-shifted by roughly 1000 cm^{-1} compared to results obtained using the more accurate and recent potentials from Ref. [42]), but this does not solve the problem of the line separation between O_h and T_d that always remains around 1000 cm^{-1} , which is half the value observed in the experiment. This indicates that more investigations are

needed to understand the disagreement between experimental and simulated positions. Clearly, high accuracy Cs-Ar potential curves are needed, and better Cs-Ar-Ar third order, especially for nearest neighbors distances, should be established.

The line position alone is a good indicator of the trapping site but is not always sufficient to determine it. If the calculated positions for the T_d 4 vacancies and O_h 6 vacancies cases are indeed compatible with the observation, it is wise to also look for the other stable trapping sites that lie as well on the convex hull: the single vacancy case with one Ar atom being substituted by a Cs atom and the 10 vacancies. The simulation of the position of the absorption lines for the single vacancy substitution site leads to theoretical lines very red-shifted located below $10\,000\text{ cm}^{-1}$ where no lines are observed experimentally. We can thus rule out this case, however the 10 vacancies case leads to line positions at $13\,760\text{ cm}^{-1}$ and $13\,210\text{ cm}^{-1}$.

In order to study the lineshape and not only the central position, we need now to add the thermal broadening of the lines due to electron-lattice interaction.

We already give the result for 1 and 10 vacancies cases in Fig. 7 in order to confirm that they can probably be ruled out because of the large shift for the 1 vacancy and the too large and inverted triplet splitting for 10 vacancies. In the following, we will therefore focus more on the 4 and 6 vacancies cases.

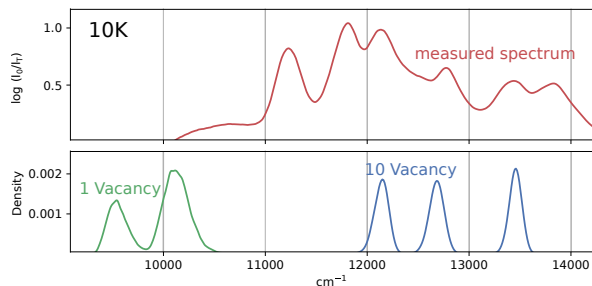


FIG. 7. Comparison between experimental absorption spectrum and theoretical semi-classical Mulliken formula (4) for the 1 and 10 vacancy sites at 10 K.

D. Lattice interaction

We need to take into account the effect that the nuclei are not at a given position due to zero point energy and temperature.

1. Electron-lattice interaction for non-equilibrium positions

We use the pair-wise potentials to calculate the electronic ground state energy $V(\mathbf{R})$ for positions of the Cs and $(N - n)$ Ar nuclei $\mathbf{R} = \{\mathbf{R}_1, \dots, \mathbf{R}_{N-n+1}\}$ around the equilibrium (\mathbf{R}_0) point found by the stability study.

Then, as detailed in the appendix C, we diagonalize the (mass-scaled) Hessian matrix, estimated by finite difference, to find the normal mode coordinates \mathbf{Q}^n . With the Hessian matrix, we have access to all oscillation frequencies; this is a more accurate way to include the zero-order effect than the Feynman-Hibbs formula used before.

2. Semi-classical approximation for the transitions

To study laser excitation of the (6s) cesium atom toward the 6p manifold, under the dipolar operator \hat{d} , we start (thanks to Beer-Lambert-Bouguer's law) by using the fact that the spectral density optical absorption coefficient $A(E)$ for a photon of energy E , is given by the sum over all initial vibronic levels $|i\rangle$, populated with probability P_i with state $|\Psi_i\rangle$ of energy E_i , towards all possible final ones $|\Psi_f\rangle$ of energy E_f :

$$A(E) \propto \sum_{f,i} P_i \left| \langle \Psi_f | \hat{d} | \Psi_i \rangle \right|^2 \delta(E - (E_f - E_i)) \quad (3)$$

$A(E)dE$ is the absorption coefficient for a photon in the energy band $E, E + dE$. Several approximations are derived in Appendix D, for instance, we neglect the variation of the dipole $d_{if}(\mathbf{Q})$ with the internuclear distances and assumed it to be constant (it is simply the 6s to 6p dipole transition). We will especially use two approximations:

$$A(E) \propto \int P_g(\mathbf{Q}) \delta[E - (V_e(\mathbf{Q}) - V_g(\mathbf{Q}))] d\mathbf{Q} \quad (4)$$

$$A(E) \propto \sum_i P_i \int |\Psi_i(\mathbf{Q})|^2 \delta[E - (V_e(\mathbf{Q}) - E_i)] d\mathbf{Q} \quad (5)$$

The first one (equation (4)) is simply called the Mulliken approximation. The second one (equation (5)) is called the Reflection approximation. $V_e(\mathbf{Q})$ is the electronic excited (6p) potential energy curve and $V_g(\mathbf{Q})$ the ground state one. $P_g(\mathbf{Q})$ can be chosen by classical statistics $P_g(\mathbf{Q}) \propto e^{-V_g(\mathbf{Q})/k_B T}$ and the formula are thus called *classical* but it is clearly better to choose the quantum-statistical mechanical probability distribution $P_g(\mathbf{Q}) = \sum_i P_i |\Psi_i(\mathbf{Q})|^2$ and in this case we called them *semi-classical*.

Depending on the derivation chosen, the classical Mulliken approximation can be derived from the Reflection one, with an additional approximation, such as in Ref. [79], whereas the reverse (reflection approximation derived from the Mulliken one), is also possible as in Ref. [80]. Therefore it is not clear which formula is the most accurate. However, proper derivation (see Appendix D) tends to favor the (semi-)classical Mulliken approximation. Indeed, the Mulliken difference potential $E - (V_e(\mathbf{Q}) - V_g(\mathbf{Q}))$ is known to be a quite good approximation for a Franck-Condon factor [81, 82] because it favors transition where the kinetic energy term is identical between ground and excited state. That is where the

phase of the ground and excited wavefunctions matches best and so favors their overlap, as also highlighted in the one-dimensional WKB approximation.

Thus, we start with the semi-classical Mulliken approximation.

We will use the Monte Carlo integration to estimate the integrals numerically. In our case, as calculated before for the line position from the spin-orbit and the interaction matrix in the $6p$ manifold, we do not have a single excited state potential curve $V_e(\mathbf{Q})$ but in Cs($6p_{1/2}, 6p_{3/2}$) manifold, 6 eigenvalues $V_{i,\text{exc}}(\mathbf{Q})$ (the degeneracy of which depends on the symmetry of the trapping sites). The spectra are thus simply given by summing the histogram of all eigenvalue cases.

3. Phonons thermal effects

At temperature T the average number of phonons with frequency ω is given by the Bose-Einstein distribution $\bar{n}_\omega = \frac{1}{e^{\hbar\omega/k_B T} - 1}$, and the probability of exciting this phonon mode with n quanta (of energy $E_n = (n + 1/2)\hbar\omega$) is given by the geometric distribution $P_n = e^{-n\hbar\omega/k_B T} [1 - e^{-\hbar\omega/k_B T}]$. In the semi-classical approximation, we use the true (quantum) probability distribution function of a harmonic phonon mode of normal mode coordinate Q_ω and of angular oscillation frequency ω given by [83] $P_\omega(T) = \frac{1}{\sqrt{2\pi\hbar[\bar{n}_\omega + 1/2]}/\omega} e^{-\frac{\omega^2 Q_\omega^2}{2\hbar\omega[\bar{n}_\omega + 1/2]}}$. Thus, if we perform the classical Mulliken calculation with a Boltzmann distribution at $T' = T'(\omega)$ such that

$$\frac{T'(\omega)}{T} = \frac{\hbar\omega}{k_B T} [\bar{n}_\omega + 1/2] = \frac{\hbar\omega}{2k_B T} \left[\tanh \frac{\hbar\omega}{2k_B T} \right]^{-1} \quad (6)$$

we will get the correct quantum spectral band contour in the approximation of harmonic motion under the $\frac{1}{2}\omega^2 Q_\omega^2$ potential as if we had done the full real quantum calculation at T . Thus a classical Mulliken simulation at T' is the same as a semi-classical Mulliken simulation at T . This scaled temperature is a way to include phenomenologically the position oscillation due to the zero point energy in classical simulations [84]. The scaled temperature was, for instance, used to study Na in Ar using Molecular Dynamic simulation in Ref. [70] where $T = 12$ K and so $T' = 45$ K was used for the pure argon subsystem that thermalizes the Na deposition on other Ar layers.

In argon, the Debye frequency is $\omega_D = k_B \times 93.3 \text{ K}/\hbar$ leading to an effective temperature of $T' \approx 44$ K at low temperature. Because we have several frequencies (one per mode), we used the scaled the temperature $T'(\omega)$ for each of them and chose the mode coordinate Q_ω accordingly to the distribution $P_\omega(T'(\omega)) \propto e^{-\frac{\omega^2 Q_\omega^2}{2k_B T'(\omega)}}$. The energy levels are then calculated for the chosen nucleus position as done previously for the equilibrium positions. A histogram for the energy difference between excited levels and the ground state one finally gives the absorption coefficient at each energy according to Eq. (4). For

this simulation, only Ar atoms within a specific cut-off distance R_c from the Cs atom are considered. For all simulations presented here, convergence is obtained for $R_c = 3$ nm. This corresponds to ~ 3000 Ar atoms, the position of which have been optimized to relax the ground state energy. However, already $R_c = 1$ nm leads to a reasonable convergence.

To benchmark our method, we compared it with Na in Ar results from [70] and found indeed very similar absorption spectra for the T_d site.

For our Cs-Ar system, calculations are done with bare two body Cs-Ar potential, but we found no effect on the shape when adding third order or when using other potentials such as from [41]. However, as discussed previously, the exact position can not be perfectly reproduced for all presented simulations. Therefore, we shift the theoretical spectra for each O_h and T_d cases.

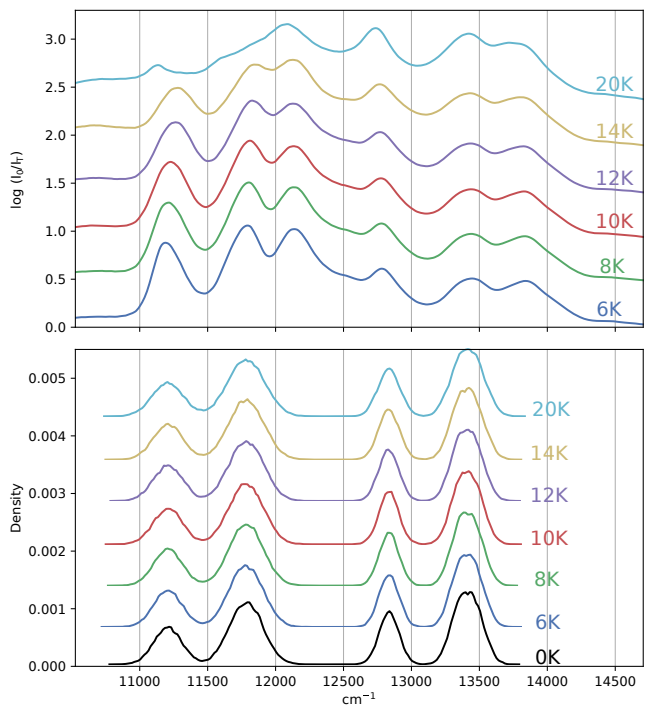


FIG. 8. Comparison between experimental absorption spectra and theoretical semi-classical Mulliken formula (eq.(4)) at different temperatures $T = 6$ K, 8 K, 10 K, 12 K, 14 K and 20 K and also for $T = 0$ K for the theory. The theoretical spectra are created from a kernel density estimation of the Monte Carlo simulation results. The results for the T_d and O_h site have been shifted in energy by a global offset to enable easier comparison with the experimental data. For better visual clarity, vertical offsets have been applied to both the experimental and the theoretical spectra.

The results for 10000 simulated samples of the semi-classical Mulliken simulations are given in Fig. 8 for the O_h and T_d cases. The experimentally observed broadening of the lines is well reproduced, but the triplets are not visible because the $6p_{3/2}$ doublet is not resolved. Furthermore, the temperature evolution is not at all reproduced

by the classical model.

The reason that almost no temperature effect arises is that we have a phonon angular frequencies spectral density very similar to the one for a pure fcc matrix so ranging from ~ 0 K to the Debye frequency ~ 94 K. So, whatever the experimental temperature $T = 6 - 14$ K the energy spanned $V_g(\mathbf{Q})$ by the ground state motion does not vary much with the temperature because the scaled temperature $T'(\omega)$ is always $T'(\omega) \approx \frac{\hbar\omega}{2k_B}$ and so not very sensitive to the actual experimental temperature.

It is interesting to note that a purely classical model using T , not T' , as done for Na in Ar in Ref. [85], is able to resolve the peak degeneracy and to show temperature effects when T varies. This is an example of a faulty model that gives erroneous results but that might, at first glance, look reasonable.

Another intriguing aspect concerns the fact that a simple Crystal Field model used in Ref. [18] was able to reproduce the triplet structure quite well. Thus, we now study this Crystal Field model based only on first-order electron-lattice interaction in order to understand why a simplification of the model might, strangely, give better results than the more complete one we just used.

4. Crystal Field: First order electron-lattice interaction

The crystal field model is based on the natural expectation that, for better physical insight, it is worth linking the motional modes to the symmetry group of a given trapping site using the so-called crystal field theory [86].

The normal modes \mathbf{Q}^n coordinates have been chosen to obtain a diagonal Hamiltonian with ground state potential energy given by $\langle 6s|\hat{V}|6s\rangle = V_0 + \sum_k \frac{1}{2}\omega_k^2 Q_k^{n2}$. However, within the Cs(6p) manifold, these coordinates \mathbf{Q}^n are not necessarily the most appropriate anymore. Indeed, if we restrict ourselves to the first order se-

ries in nuclear coordinates, each of the 9 coefficients $V_{m',m} = \langle 6pm'|\hat{V}|6pm\rangle$ of the interaction matrix (2), when summed over all Ar positions, contains only linear combinations of the \mathbf{Q}^n . Thus, at most 9 different so-called interaction modes matter, each of them being a linear combination of the normal modes. These interaction modes are much more appropriate than the normal modes to give a physical insight of the Cs(6p) interaction within the Ar matrix.

They can be calculated when the interactions, so the potential curves, are known. But, in the crystal field theory the $Q_{\Gamma\gamma}$ interaction mode coordinates are simply predicted using the symmetries of the trapping site. A given trapping site is an element of a symmetry group with irreducible representations Γ (and its row γ). From it we find the $Q_{\Gamma\gamma}$, that are the linear combination of the normal modes invariant under the Γ symmetries. The symmetries are also reflected on the electronic wavefunction that should have an adapted basis set $|\Gamma\gamma\rangle$. Finally, the electron-lattice interaction can be written at first order (so-called crystal-field approximation) as $H_{CF} = V^{(0)}(\mathbf{r}) + \sum_{\Gamma\gamma} V_{\Gamma\gamma}^{(1)}(\mathbf{r})Q_{\Gamma\gamma}$.

If we focus on the 6p manifold. The symmetries for the zero-order $V^{(0)}(\mathbf{r})$ potential indicates, in the cubic O_h case, that $\Gamma = T_{1u}$ and the adapted electronic basis $|\Gamma\gamma\rangle$ is simply the 6p real (tesseral) spherical harmonics $|x\rangle, |y\rangle, |z\rangle$. Similarly $\Gamma = T_1$ in the T_d case. Now, to evaluate the first-order term $\sum_{\Gamma\gamma} V_{\Gamma\gamma}^{(1)}(\mathbf{r})Q_{\Gamma\gamma}$ in this basis we use of the Wigner-Eckart-theorem [87–89] $\langle \Gamma_1\gamma_1|V_{\Gamma\gamma}^{(1)}|\Gamma_2\gamma_2\rangle = \langle \Gamma_1||\hat{V}_\Gamma^{(1)}||\Gamma_2\rangle \langle \Gamma_1\gamma_1|\Gamma_2\gamma_2, \Gamma\gamma\rangle$. It gives the selections rules and predicts the non-zero coefficients $\langle \Gamma_1\gamma_1|V_{\Gamma\gamma}^{(1)}|\Gamma_2\gamma_2\rangle$ that occur only for some $Q_{\Gamma\gamma}$ [90–92]. The details of the calculation are given in appendix A for several symmetry-groups in the $|x\rangle, |y\rangle, |z\rangle$ basis. For better comparison with the previous calculation, we give it here in the $|m\rangle = |-1, 0, +1\rangle$ basis, where the hamiltonian matrix M_{CF} (see Eq. (A1) for the T_d case is given by

$$\begin{pmatrix} V_{A_1}Q_{A_1} - \frac{V_E Q_{E,2}}{\sqrt{3}} & V_{T_2} \frac{iQ_{T_2,1} + Q_{T_2,2}}{\sqrt{2}} & -V_E Q_{E,1} - iV_{T_2} Q_{T_2,3} \\ V_{T_2} \frac{-iQ_{T_2,1} + Q_{T_2,2}}{\sqrt{2}} & V_{A_1}Q_{A_1} + 2\frac{V_E Q_{E,2}}{\sqrt{3}} & V_{T_2} \frac{-iQ_{T_2,1} - Q_{T_2,2}}{\sqrt{2}} \\ -V_E Q_{E,1} + iV_{T_2} Q_{T_2,3} & V_{T_2} \frac{iQ_{T_2,1} - Q_{T_2,2}}{\sqrt{2}} & V_{A_1}Q_{A_1} - \frac{V_E Q_{E,2}}{\sqrt{3}} \end{pmatrix} \quad (7)$$

For O_h , the results are the same, only the name of the symmetries slightly changed, but for simplicity we keep these notations in the following for both T_d and O_h . Comparison with the matrix (2) gives a physical insight. The A_1 mode (Q_{A_1} varying as $X^2 + Y^2 + Z^2$) is a symmetrical radial one that preserves the symmetry, the E_g mode ($Q_{E,1}$ varying as $X^2 - Y^2$ and $Q_{E,2}$ as $2Z^2 - X^2 - Y^2$) is a tetragonal distortion that for instance modify the O_h symmetry into D_{4h} and T_2 ($Q_{T,1}, Q_{T,2}, Q_{T,3}$ varying respectively as XZ, YZ or XY) bends the crystal to D_{3d}

or C_{3v} .

We note that if the matrix elements are linear in the interaction mode coordinates, the eigenvalues, which are the potential curves, are not. Thus, to calculate the Cs(6s-6p) absorption spectra, we cannot use the analytical formula (see for instance [79, 93]) for the case where the slope of each curve is a linear function of the mode. A Monte Carlo simulation (or another numerical integration method) is still needed to calculate the absorption spectra. In the Mulliken formula 4 we

have $V_g(\mathbf{Q}) = V_{\text{Cs}(6s)-\text{Ar}}(\mathbf{Q}) + V_{\text{Ar}-\text{Ar}}(\mathbf{Q})$ and $V_e(\mathbf{Q}) = V_{\text{Cs}(6p)-\text{Ar}}(\mathbf{Q}) + V_{\text{Ar}-\text{Ar}}(\mathbf{Q})$ so

$$V_e(\mathbf{Q}) - V_g(\mathbf{Q}) = V_{\text{Cs}(6p)-\text{Ar}}(\mathbf{Q}) - V_{\text{Cs}(6s)-\text{Ar}}(\mathbf{Q}) \quad (8)$$

Because in the crystal field linear approximation $V_{\text{Cs}(6s)-\text{Ar}}(\mathbf{Q}) = 0$ (or constant that we offset), Eq. (4) simply becomes

$$A(E) \propto \int \sum_{i=1}^6 \delta[E - X_i(\mathbf{Q}^\Gamma)] e^{-\sum_{\Gamma\gamma} \omega_\Gamma^2 Q_{\Gamma\gamma}^2 / 2k_B T} d\mathbf{Q}^\Gamma \quad (9)$$

where $X_i(\mathbf{Q}^\Gamma)$ are the eigenvalues of M_{CF} plus the spin-orbit matrix (A2), $A^{\text{SO}} \mathbf{L} \cdot \mathbf{S}$. This can be estimated using a Monte Carlo method such that each $\frac{\omega_\Gamma Q_{\Gamma\gamma}}{\sqrt{k_B T}}$ follows a standard unit normal Gaussian distribution [92].

Here we have assumed, in the Boltzmann distribution, that the ground state energy can be written as $V_g(\mathbf{Q}) = \frac{1}{2} \sum_{\Gamma\gamma} \omega_\Gamma^2 Q_{\Gamma\gamma}^2$. This is obviously not the case because the $Q_{\Gamma\gamma}$ are not the normal mode coordinates. However, we have checked that in our study of the $6s - 6p$ transition, if projected to the sole $Q_{A_1}, Q_{E,1}, Q_{E,2}, Q_{T,1}, Q_{T,2}, Q_{T,3}$ "active" coordinates the ground state, Hamiltonian is indeed of this desired quadratic diagonal form. In this case, as used in Ref. [91, 92] (see discussion in Appendix C 3), the oscillations frequencies ω^Γ are not needed for the Mulliken semi-classical case, because we can include them in the definition of new scaled coordinates $\tilde{Q}_{\Gamma\gamma} = \frac{\omega_\Gamma}{\sqrt{2}} Q$ with new interaction coefficients $\tilde{V}_{\Gamma\gamma} = \frac{\sqrt{2}}{\omega_\Gamma} V$, such that $V_{\Gamma\gamma} Q_{\Gamma\gamma} = \tilde{V}_{\Gamma\gamma} \tilde{Q}_{\Gamma\gamma}$; so with Eq. (9) becoming

$$A(E) \propto \int \sum_{i=1}^6 \delta[E - X_i(\tilde{\mathbf{Q}}^\Gamma)] e^{-\sum_{\Gamma\gamma} \tilde{Q}_{\Gamma\gamma}^2 / k_B T} d\tilde{\mathbf{Q}}^\Gamma \quad (10)$$

Usually, the crystal field theory is used only as an effective theory. In other words, the parameters $\tilde{V}_{\Gamma\gamma}$ are adjusted to the data by knowing the trapping site symmetry. This fit, along with the $6s$ offset for the line position and possibly the fine structure splitting, usually leads to a very good agreement between experiment and theory because of the large number of free parameters.

This crystal field method is orders of magnitude faster than previously discussed Monte Carlo, or than a molecular dynamics calculation, where all Gaussian random distribution of the atoms that move and their interactions with all other atoms have to be calculated. The crystal field method required only few parameters ($\tilde{V}_{A_1}, \tilde{V}_E, \tilde{V}_{T_2}$ in our case), very few Gaussian random distributions ($\tilde{Q}_{A_1}, \tilde{Q}_{E,1}, \tilde{Q}_{E,2}, \tilde{Q}_{T,1}, \tilde{Q}_{T,2}, \tilde{Q}_{T,3}$ in our case). Furthermore, the interaction is simply given by the analytical matrix (7).

It is therefore a very attractive method. Furthermore, as mentioned before, in Ref. [18] the two observed triplets (very similar to our experimental data) were attributed to cubic symmetry sites and quite well fitted using the matrix (7) with parameters that we recall in table I. The

fit was done classically, assuming a temperature of $T = 1.8$ K (without any temperature scaling). Indeed, Using these crystal field parameters, the calculated line shapes $A(E)$ from (10) match quite well the observed shape, and the triplet structure can be resolved. Using different $\tilde{V}_{A_1}, \tilde{V}_E, \tilde{V}_{T_2}$ parameters for the two sites can even lead to an almost perfect match.

Site modes	O_h			T_d		
	A_1	E	T_2	A_1	E	T_2
$\hbar\omega_\Gamma/k_B$	60	75	65	64	68	72
$(V_\Gamma/\omega_\Gamma)^2/k_B$	50	120	140	110	130	150
$(V_\Gamma/\omega_\Gamma)^2/k_B$ from [18]	13600	84700	12600	13600	84700	12600

TABLE I. Crystal field parameters, given in Kelvin, for the two types of sites. Oscillation frequencies are such that the ground state potential is given by $\langle 6s | \hat{V} | 6s \rangle = V_0 + \sum_{\Gamma\gamma} \frac{1}{2} \omega_\Gamma^2 Q_{\Gamma\gamma}^2$ and the V_{A_1}, V_E, V_{T_2} are the coupling parameters for the excited state matrix (7) that has linear terms of the $V_\Gamma Q_{\Gamma\gamma}$ type. The values empirically inferred from an experimental spectrum in Ref. [18] are given for comparison.

However, we can also calculate the coefficients V_{A_1}, V_E, V_{T_2} , by comparing the matrix (7) to the gradient of the interaction matrix calculated using the summation of Cs-Ar potentials (see details in Appendix C and formulas (C2) and (C3)). The parameter $(V_\Gamma/\omega_\Gamma)^2$ has a physical meaning of a Jahn-Teller energy shift for the excited potential, because of the formula $V_\Gamma Q_{\Gamma\gamma} + \frac{1}{2} \omega_\Gamma^2 Q_{\Gamma\gamma}^2 = \frac{1}{2} \omega_\Gamma^2 \left(Q_{\Gamma\gamma} + \frac{V_\Gamma}{\omega_\Gamma^2} \right)^2 - \frac{1}{2} \frac{V_\Gamma^2}{\omega_\Gamma^2}$. Results are given in table I where to have a better idea of the value of the frequencies ω_Γ and of the interaction coefficients V_Γ we give both in temperature units using $\hbar\omega_\Gamma/k_B$ and $(V_\Gamma/\omega_\Gamma)^2/k_B$.

The V_Γ parameters found using realistic interaction potential are totally different from those fitted in Ref. [18]. This illustrates the fact that fitting crystal field parameters alone may not reflect any physical reality and in turn leads to quite inaccurate results that can then produce misleading predictions for other studies [94]. It is thus essential to test them with another independent study such as magnetic circular dichroism (MCD) [94] temperature dependence of the absorption lines or as we did compare them to theoretical predictions [95–98].

However, it is important to stress that if we use our V_{A_1}, V_E, V_{T_2} coefficients, that is, if we restrict our absorption band shape Mulliken semi-classical simulation to the first order in the \mathbf{Q}^Γ coordinates for the excited state interaction matrix, these crystal field results are almost identical to the full Monte Carlo classical simulation performed in Fig. 8, where the excited states are calculated from the full potentials. Indeed, for our temperature range, the first-order matrix element values found in the Monte Carlo simulation are less than 10% off relative to the real ones.

In conclusion, the full potentials, or only the crystal field first order approximation for the excited state matrix coefficients, are almost identical but can not reproduce the triplet structure we observe nor its temperature

evolution. The problem might arise from the classical model for the ground state motion that does not hold at low temperatures where the vibrational energies are quantized.

5. Reflection approximation and quantization of the energy

The classical simulations, even with temperature scaling using the proper spatial Gaussian distribution $\Psi_i(\mathbf{Q})$, are intrinsically incorrect because they use a continuous energy $P_g(\mathbf{Q})$ in Eq. (4) where real system have quantized energy E_i in the ground state. In the extreme case of single zero phonon mode occupation (low temperature), the motional ground state has only a single energy, whereas the classical simulation allows all energies from 0 to this zero-point energy. This illustrates that the classical simulation is able to produce an artificial broadening of the lines on the order of half the Debye oscillation frequency, so in Ar on the order of $\sim 30 \text{ cm}^{-1}$ per vibrational (phonon) modes. Obviously, this is quite an extreme case, because almost all lattice vibrations are similar between ground and excited states, and thus the potential difference given by Eq. (8) is almost zero; only few lattice vibrations, linked to the A, E, T_2 crystal field modes, can be strongly modified by the electronic excitation. However, this can qualitatively explain why our classical simulation fails to produce a triplet structure and produces a broad doublet. Thus, the semi-classical Mulliken approximation, which is primarily used to simulate atomic spectra in rare gas matrices [45, 52, 70, 71, 85], might be inappropriate in our case [99]. Indeed, it was shown that for the $A \rightarrow T$ spectral band shape ($6s \rightarrow 6p$ is $A_{1g} \rightarrow T_{1u}$ for O_h or $A_1 \rightarrow T_1$ for T_d) the semi-classical Mulliken approximation cannot account for the observed line shapes, especially at low temperatures [99–101].

In most experiments performed with cryogenic rare gas matrices, a large majority of phonon modes have much higher energies than the thermal one $\hbar\omega \gg k_B T$. Thus, the vibronic transitions often occur from the zero-phonon occupation, as observed, for instance, with heavy atoms like Eu, Sm, or Yb in Ar [102–106]. These cases are similar to our case if restricted to of a single A_1 mode where the harmonic potential $\frac{1}{2}\omega_{A_1}^2 Q_{A_1}^2$ in the ground state is displaced (due to the linear $V_{A_1} Q_{A_1}$ term) in the excited states where vibrational quantization produces well resolved (Huang Rhys Pekar types of) peaks [107–110]. These peaks can obviously only be explained in a full quantum treatment of the kinetic energy and not by a semi-classical Franck-Condon-Mulliken approximation.

Our case is the so-called $T \otimes (a + e + t_2)$ coupling (6p triplet T coupled with the lattice through Q_{A_1} in a A_1 mode, $Q_{E,1}, Q_{E,2}$ in a E_g mode and $Q_{T,1}, Q_{T,2}, Q_{T,3}$ in a T_2 mode) plus spin-orbit. It is extremely complex but strongly linked to the Jahn-Teller $T \otimes (e + t_2)$ coupling that has been extensively studied with full quantum mechanical treatments tackled using many approximations

of weak or strong coupling V_Γ compared to the oscillation frequency ω_Γ , with or without spin-orbit interaction, with only nearest neighbors (so-called cluster model) or with full lattice, using second-order perturbation theory, with adiabatic potential curves and tunneling effects... [93, 96, 101, 111–113]. Even with some approximations, quite valid in our case see Table I, of a p state equally coupled to E and T vibrations [99] the problem is very complex. But, in this case, the full quantum treatment [114] seems to agree with the classical one of Ref. [92].

The only way to get a definitive answer would thus be to perform a full quantum calculation of the nuclear motion in the calculation of the probability transfers. It is clearly way beyond the scope of this article where we would like to use simple semi-classical expressions for the calculation of electronic absorption spectra without having to calculate the molecular vibrational eigenstates.

In our case most of the phonon energies $\hbar\omega$ and the Jahn-Teller energy shifts $\hbar(V_\Gamma/\omega_\Gamma)^2$ are larger than the kinetic energy temperature $k_B T$. Thus, the reflection approximation of Eq. (5) should be more accurate than the Franck-Condon Mulliken approximation because the excited-state oscillator can be treated classically when the ground state is quantized [79, 108]. Unfortunately, the use of the reflection approximation leads to many difficulties because using the harmonic approximation $V_g(\mathbf{Q}) = V_{\text{Cs}(6s)-\text{Ar}}(\mathbf{Q}) + V_{\text{Ar}-\text{Ar}}(\mathbf{Q}) = \sum_k \frac{1}{2}\omega_k^2 Q_k^{n^2}$ shows that we have to calculate $V_e(\mathbf{Q}) - E_i = V_{\text{Cs}(6p)-\text{Ar}}(\mathbf{Q}) - V_{\text{Cs}(6s)-\text{Ar}}(\mathbf{Q}) + \sum_k \frac{1}{2}\omega_k^2 Q_k^{n^2} - E_i$, where the total quantized ground state energy $E_i = \sum_k \hbar\omega_k(n_k + 1/2)$ and $\sum_k \frac{1}{2}\omega_k^2 Q_k^{n^2}$ both grow linearly with the number of modes. We can circumvent this non-physical divergence by separating the modes into "passive" or "active" depending if they affect $V_{\text{Cs}(6p)-\text{Ar}}(\mathbf{Q}) - V_{\text{Cs}(6s)-\text{Ar}}(\mathbf{Q})$ or not using the symmetry adapted coordinates where only the 6 active coordinates strongly modify the Cs interaction with the Ar crystal.

Unfortunately, the ground state Hamiltonian is no longer diagonal in the interaction modes, and so the energy is not well defined. To solve this problem, we will use the fact that in the low temperature regime the soft normal coordinates phonons modes with low frequency $\omega \gtrsim k_B T/\hbar$ are populated, producing a different spatial distribution for these normal modes and so for their linear combinations that are present in the 6 interaction mode coordinates. A simple way to treat this is, for each temperature T , to scale each normal mode frequency by changing ω in ω' such that $\omega'^2/T = \omega^2/T'(\omega)$ to keep the correct spatial distribution for the normal modes. The orthonormal transformation thus produced some new diagonal $\omega'_{\Gamma\gamma}(T)$ oscillation frequencies for the 6 interaction modes coordinates. We thus simulate for this temperature T a spectrum by using the classical Boltzmann distribution $\propto e^{-\frac{1}{2}\omega'_{\Gamma\gamma}(T)^2 Q_{\Gamma\gamma}^2/k_B T}$ for each $Q_{\Gamma\gamma}$ and a classical energy $E_i = \sum_{\Gamma\gamma} \frac{1}{2}\omega'_{\Gamma\gamma}(T)^2 Q_{\Gamma\gamma}^2$. The formula

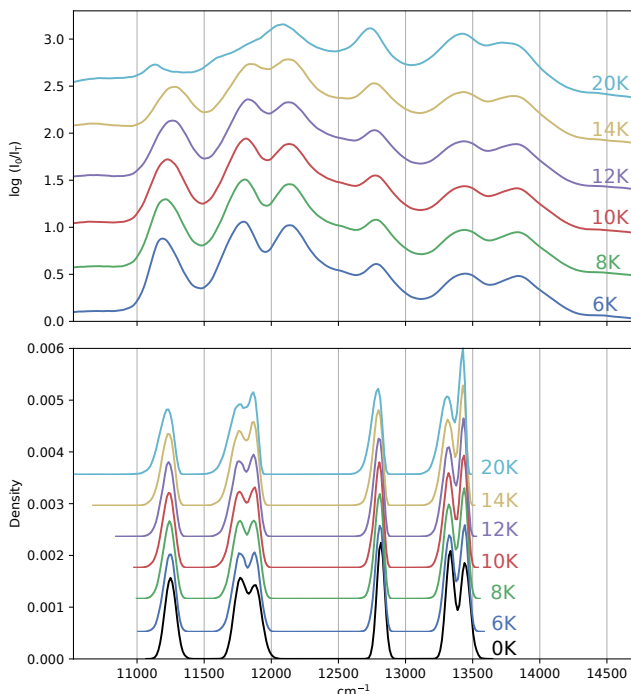


FIG. 9. Comparison between the observed absorption and the simulated one using the temperature scaled first order crystal fields model with the modified reflection approximation of Eq. (11) using parameters of Table I. The theoretical spectra are created from a density kernel estimation of the Monte Carlo simulation results. The results for the T_d and O_h site have been shifted in energy by a global offset to enable easier comparison with the experimental data. For better visual clarity, vertical offsets have been applied to both the experimental and the theoretical spectra.

used is thus, with \mathbf{Q} the interaction mode coordinates,

$$A(E) \propto \sum_i P_i \int |\Psi_i(\mathbf{Q})|^2 \delta[E - (V_{\text{Cs}(6p)} - A_r(\mathbf{Q}) - \sum_k \frac{1}{2} \omega_k'^2 Q_k^2)] d\mathbf{Q} \quad (11)$$

Results are presented in Fig. 9. This (modified) reflection approximation restores the triplet shapes. Unfortunately, the splittings are not very close to the observed one at the lowest temperature of $T = 6$ K. Furthermore, the simulated spectra show some evolution with temperature that does not fully agree with the observed one. Since one has to be careful about the experimental temperature calibration due to the fact that the temperature of a matrix sample may differ from the temperature of a nearby sensor [115], we cannot expect perfect agreement. However, there are more important discrepancies that remain. The most important one being probably the fact that the splitting between the peaks does not match the experimental one. Furthermore, experimentally the red trapping site, which we attribute to O_h , and the blue

trapping site, we attribute to T_d behaves, differently with temperature, whereas the simulation predicts a similar behavior for O_h or T_d sites simply because in both cases the $\text{Cs}(6p)$ interaction with the Ar matrix is governed by similar couplings as shown by the similar values for the coupling coefficients in Table I (the different V_{A_1} values are not of great importance because the A_1 mode simply convolutes the lineshapes [92]).

It is thus not clear that using better approximations for the absorption shape tzz would help. Among such improved approximations, we can nevertheless cite the improved crystal field absorption lineshape formula proposed in Ref. [100] where the S-P transitions are calculated for the most general case, where the coupling of all three vibration modes A_1, E_g, T_2 , as well as spin-orbit interaction, are considered. But because the ω_T frequencies are almost identical for the T_d and O_h case, this interesting formula can not produce a different temperature evolution for the two sites. Furthermore, as stressed in Ref. [116], in general, if a semi-classical formula indeed requires correction when the energy involved is on the order of the quantization energy spacing, the proposed corrected terms

obtained based on \hbar power expansion in phase space [80, 117–123] (some are mentioned in the appendix D) have a similar order of magnitude, and so convergence is not clear. So, they will probably not solve the problem of the similar predicted T_d and O_h behaviors.

It may be more promising to look for other effects to solve this discrepancy, such as to look for non-Born-Oppenheimer effects like nonadiabatic coupling.

IV. CONCLUSION

In conclusion, we have observed Cs absorption spectra in an Ar matrix containing 6 major resonances. These were assigned to transitions of the $6s_{1/2}$ Cs ground state towards $6p_{1/2}$ and $6p_{3/2}$ excited states with lifted $|m|$ -degeneracy and two different trapping environments. Pairwise Ar-Ar and Cs-Ar potentials allow a stability study that tends to indicate that the two triplets observed are due to a 4 vacancy tetrahedral T_d trapping site and to a 6 vacancies cubic O_h one in an fcc Ar matrix. In order to qualitatively reproduce the line locations by the pairwise approach, we have properly derived effective two-body potential curves to include zero-point energy and third-order terms. We found that zero-point energy has a minor effect but that adding third-order many-body corrections modifies the potentials significantly. Our derivation of the effective two-body potential from the long-range part of the triple dipolar interaction, based on an exact derivation of the long-range part, is not very accurate. Clearly, more work is needed on effects such as the Pauli repulsion, exchange interaction and three-body dispersion interactions for the rare gases - alkali atoms, especially in excited states and for the short-range part [124].

Our study reasonably assigns the almost unshifted (in relation to the gas phase) triplet to the 4 vacancy T_d , and the blue-shifted one to the 6 vacancies cubic O_h trapping site. The use of the computationally more demanding core polarization pseudopotentials will be an interesting approach to confirm this fact and to find better agreement between theory and experiment for the line separations [71, 125].

Within the present approach, we show that a triplet shape can only be reproduced by using quantized energy for the ground state vibrational motions. Indeed, the classical simulation might produce artificial broadening of the lines on the order of half the Debye oscillation frequency, so in Ar on the order of $\sim 30\text{cm}^{-1}$. Thus our classical Semi-classical Mulliken simulation fails to produce a triplet structure and produces a broad doublet. A simulation using the reflection approximation, on the other hand, only produces a triplet at 0K, but otherwise diverges when increasing the number of Ar atoms due to an unphysical treatment of the phononic modes. Finally, a quantized simulation based on a modified reflection approximation reproduces a triplet structure and shows that modifying the population of the soft (low frequency) phonon modes can also modify the absorption shapes. We also show that using only the matrix gradient (linear, first-order approximation) for the excited state does not alter the quality of the results but leads to way faster calculations. Furthermore, for low temperatures, when only ground state vibrational (zero-phonon) levels are populated, the important result is that the fastest and simplest crystal field model is quite sufficient to reproduce the observed line broadening produced by the dynamical Jahn-Teller thermal effect. It requires only three electron-lattice parameters given in Table I (together with Eq. (9) and diagonalization of spin-orbit and (7) matrices) [92]. Such a reduced number of modes is beneficial. First, because it leads to much faster calculations than the full Monte Carlo method using motions and interactions of all the atoms. Secondly, which may be more important, it captures the essential aspects of the electrostatic interaction and is thus a very powerful starting point for further studies including for instance the hyperfine structure or the magnetic circular dichroism (MCD).

This work was, however, neither able to reproduce the triplet splitting nor did it give the right red and blue line separation. The reason for the discrepancy is unclear, but we can note that we neglect the dipole transition dependence with the Q coordinates, ignore coupling with other excited states (like Cs(5d)), have not appropriately included the third-order non-additive terms in the potentials. The role of nonadiabatic couplings should also be studied.

Following [70], it might be interesting to modify the potential curves, such as the $B\Sigma$ state which was recently suspected to be inaccurate [126], in order to create better agreement between experiment and theory. However, our first attempts tends to indicate that quite a substantial modification of the position and the slope of the curve in the region near the first nearest neighbors (see Fig. 6) is required. This should be nonetheless further investigated, together with experimental and theoretical studies of other possibilities such as trapping in other crystal defects of lower symmetry, for instance 5 vacancy of D_{3h} symmetry in the hcp phase [5, 6], which may explain the discrepancy between experiment and simulation. Fortunately, experimentally many tools are available such as using for instance temperature dependence, magnetic circular dichroism, fluorescence, electron (paramagnetic) spin resonance, oscillator strength determination, time-resolved emission spectra, nonradiative branching ratios, optical pumping or bleaching studies. It is also probably interesting to study the rubidium case to compare with Cs and to use other rare gases, or even mixed ones [127], to check that the matrix shift seen in the S-P transitions is approximately linear with the polarizability of the matrix host [52, 70, 128].

We hope that our work will be useful for further studies of similar systems used for fundamental physics in rare gas solid crystals [129–131].

V. ACKNOWLEDGEMENTS

T.B. and S.L. contributed equally to this work.

This research was financed in whole or in part by Agence Nationale de la Recherche (ANR) under the project ANR-21-CE30 -0028-01.

A CC-BY public copyright license has been applied by the authors to the present document and will be applied to all subsequent versions up to the Author Accepted Manuscript arising from this submission, in accordance with the grant's open access conditions.

We acknowledge W. Chin, B. Darquier, O. Dulieu, B. Gervais, H. Lignier, Ch. Malbrunot, C. Smai, B. Viarier, and A. Voute for fruitful discussions, and B. Vivan and L. Marriaux for the design and mechanical realization.

Appendix A: Perturbation matrices for different symmetries

A given trapping site is defined by the near neighbor environment of the impurity atom and by its overall crystal orientation in the laboratory frame. We detail here the crystal field method we use to simulate the absorption spectrum.

Using vector notation for the cartesian coordinate of each position of the Cs and the $N - n$ Ar nuclei $\mathbf{R} = \{\mathbf{R}_1, \dots, \mathbf{R}_{3(N-n+1)}\}$ and \mathbf{r} as the Cs valence electron

coordinates, the electron-lattice interaction can be written as $V = V(\mathbf{r}, \mathbf{R})$, where for simplicity, we use, in this article, the same notation for operators and their representations in coordinate basis.

1. Crystal field interpretation

A given single trapping site, at the equilibrium position \mathbf{R}_0 , possesses a certain symmetry group with irreducible representation Γ (and its row γ). So it is more convenient to use coordinates, $Q_{\Gamma\gamma}$, that transforms well under such a representation. They are linear combinations of the $R_i - R_{0i}$ ones, such that at a linear (first order) approximation, in the nuclear coordinate \mathbf{R} or \mathbf{Q}^Γ , the electron-lattice interaction can be written as $\hat{V} = V^{(0)}(\mathbf{r}) + \sum_{\Gamma\gamma} V_{\Gamma\gamma}^{(1)}(\mathbf{r})Q_{\Gamma\gamma}$. We refer to this expression as the "crystal-field approximation".

At zero order, the electron lattice $V^{(0)}(\mathbf{r}) = V(\mathbf{r}, \mathbf{R}_0)$ modifies the Cs electron wavefunction throughout the $\langle n_1 l_1 m_1 | V^{(0)} | n_2 l_2 m_2 \rangle$ couplings (we use here the non-relativistic wavefunctions, without fine structure that depend on the spherical harmonics Y_l^m). The trapping site equilibrium position \mathbf{R}_0 determines the symmetry group for the nuclear environment that produces the electron lattice interaction $V_0(\mathbf{r})$. For simplicity, we keep the same notation, as for the nuclear coordinate representation Γ , and name the eigenstates of the electronic Hamiltonian that are linear combinations of the $|nlm\rangle$ states, $|\Gamma\gamma\rangle$. They are given by the projection operators for the irreducible representation Γ .

Once the Cs electronic eigenstates $|\Gamma\gamma\rangle$, that are adapted for the ground state equilibrium position, are found, we can use them to calculate the next order of the electron lattice interaction $\sum_{\Gamma\gamma} V_{\Gamma\gamma}^{(1)}(\mathbf{r})Q_{\Gamma\gamma}$.

The key result [87, 88] is that the $\langle \Gamma_1 \gamma_1 | V_{\Gamma\gamma}^{(1)} | \Gamma_2 \gamma_2 \rangle$ coupling terms can be calculated using the Wigner-Eckart's theorem $\langle \Gamma_1 \gamma_1 | V_{\Gamma\gamma}^{(1)} | \Gamma_2 \gamma_2 \rangle = \langle \Gamma_1 || \hat{V}_\Gamma^{(1)} || \Gamma_2 \rangle \langle \Gamma_1 \gamma_1 | \Gamma_2 \gamma_2, \Gamma\gamma \rangle$. Non zero Clebsch-Gordan coefficient $\langle \Gamma_1 \gamma_1 | \Gamma_2 \gamma_2, \Gamma\gamma \rangle$ occurs only if the Γ representation is part of the $\Gamma_1 \times \Gamma_2$ representation [87, 88]. Since V is real, we only need to consider the symmetric part of the product: $[\Gamma_1 \times \Gamma_2]$.

Thus, group theory automatically leads to the proper basis $|\Gamma\gamma\rangle$ and provides directly the useful representations Γ with non-zero matrix elements $V_\Gamma = \langle \Gamma_1 || \hat{V}_\Gamma^{(1)} || \Gamma_2 \rangle$ and the Clebsch-Gordan coupling coefficients.

We will now illustrate this crystal field procedure for several possible trapping site symmetries that might occur for atoms in matrices [50, 53–63]. For this we use the free Mathematica group theory package GTPack [89, 132].

2. Cubic: O_h or T_d symmetry

In fcc crystals, the 1 vacancy substitution and the 6 vacancies site both have O_h symmetry (same symmetry as the SF_6 molecule) while the 4 vacancies site has a T_d symmetry (as CH_4).

For such symmetries, the electron-lattice potential at equilibrium $V^{(0)}(\mathbf{r})$ does not lift the 6s nor the 6p degeneracy. This can be understood in a simple manner by decomposing it in spherical harmonics: $V^{(0)}(\mathbf{r}) = \sum_{l,m} r^l a_l^m Y_l^m(\theta, \varphi)$. We now only have to take into account that this interaction potential has necessarily the same O_h or T_d symmetry as the nuclear position that creates it. Thus most of the terms are zero, and the potential becomes $V^{(0)}(\mathbf{r}) = a_0 Y_0^0 + r^4 a_4 (Y_4^{-4} + \sqrt{14/5} Y_4^0 + Y_4^4) + \dots$ (a_0 is not to be confused with the Bohr radius). These leading order terms formed the so-called Devonshire's potential [133]. The triangle inequality $|l_1 - l_2| \leq l \leq l_1 + l_2$ for the Clebsch-Gordan coefficients appearing when calculating $\langle n_1 l_1 m_1 | V^{(0)} = \sum_{l,m} r^l a_l^m Y_l^m | n_2 l_2 m_2 \rangle$ indicates that the $l \geq 4$ terms cannot couple to 6s ($l = 0$) nor to 6p ($l = 1$) states but would lift the degeneracy of the 5d ($l = 2$) level for instance.

For completeness, we indicate that the same calculation can be done elegantly using directly the quantum states $|nlm\rangle$, without using spherical harmonics, by directly writing the potential $\hat{V}(\mathbf{r}, \mathbf{R}_0)$ using angular momentum operators. For this, we simply have to replace, in the Devonshire's potential expression, $Y_0^0 \rightarrow 1$, $Y_4^{\pm 4} \rightarrow L_\pm^4$ and $Y_4^0 \rightarrow 35L_z^4 - (30L(L+1) - 25)L_z^2 + 2L^2(L+1)^2 - 6L(L+1)$ where \mathbf{L} is the orbital angular momentum operator [134, 135].

It would be possible to use the $|6sm = 0\rangle$ and $|6pm\rangle = |m\rangle$ basis but for cubic symmetry the so-called real (or tesseral) spherical harmonics: $|x\rangle = (|m = -1\rangle - |m = +1\rangle)/\sqrt{2}$, $|y\rangle = i(|m = -1\rangle + |m = +1\rangle)/\sqrt{2}$, $|z\rangle = |m = 0\rangle$ is better. Indeed, the projection operator technique for the angular momentum basis $|6pm\rangle$ under the symmetry group O_h or T_d and their representations Γ leads to the following: for the 6s electronic state $\Gamma = A_{1g}$ (or $\Gamma = A_1$ for T_d) and $|6sm = 0\rangle$ forms a good basis. For the 6p electronics state $\Gamma = T_{1u}$ (or $\Gamma = T_1$ in the T_d case) and the basis $|\Gamma\gamma\rangle$ is just given by $|x\rangle$, $|y\rangle$, $|z\rangle$.

Now that the zero-order symmetry $|\Gamma\gamma\rangle$ basis adapted to the nuclear equilibrium configuration is established, we can use it to calculate the first-order correction $\sum_{\Gamma\gamma} \langle \Gamma_1 \gamma_1 | V_{\Gamma\gamma}^{(1)}(\mathbf{r}) | \Gamma_2 \gamma_2 \rangle Q_{\Gamma\gamma}$. Only the non zero $\langle 6p = T_{1u} || V^{(1)} || 6p = T_{1u} \rangle$ terms are interesting. Then because $[T_{1u} \times T_{1u}] = A_{1g} \oplus E_g \oplus T_{2g}$ (or $[T_1 \times T_1] = A_1 \oplus E \oplus T_2$ in the T_d case), the $\langle \Gamma_1 \gamma_1 | V_{\Gamma\gamma}^{(1)} | \Gamma_2 \gamma_2 \rangle Q_{\Gamma\gamma}$ calculation leads to the matrix (with the u, g label removed in the T_d case), in the 6p manifold, for the total $\langle \Gamma_1 \gamma_1 | \hat{V} = V^{(0)} + V^{(1)} | \Gamma_2 \gamma_2 \rangle Q_{\Gamma\gamma}$ crystal field (CF) interaction:

$$M_{\text{CF}} = \left(\frac{a_0}{\sqrt{4\pi}} + V_{A_{1g}} Q_{A_{1g}} \right) \mathbf{I}_3 + \begin{pmatrix} |x\rangle & |y\rangle & |z\rangle \\ V_{E_g} \left(Q_{E_g,1} - \frac{1}{\sqrt{3}} Q_{E_g,2} \right) & V_{T_{2g}} Q_{T_{2g},3} & V_{T_{2g}} Q_{T_{2g},2} \\ V_{T_{2g}} Q_{T_{2g},3} & -V_{E_g} \left(Q_{E_g,1} + \frac{1}{\sqrt{3}} Q_{E_g,2} \right) & V_{T_{2g}} Q_{T_{2g},1} \\ V_{T_{2g}} Q_{T_{2g},2} & V_{T_{2g}} Q_{T_{2g},1} & V_{E_g} \frac{2}{\sqrt{3}} Q_{E_g,2} \end{pmatrix} \quad (\text{A1})$$

Where we have used $V_{A_1} = \langle \Gamma_1 | \hat{V}_{A_1}^{(1)} | \Gamma_2 \rangle / \sqrt{3}$, $V_{E_g} = \langle \Gamma_1 | \hat{V}_{E_g}^{(1)} | \Gamma_2 \rangle / \sqrt{2}$, $V_{T_{2g}} = \langle \Gamma_1 | \hat{V}_{T_{2g}}^{(1)} | \Gamma_2 \rangle / \sqrt{2}$ and performed a orthonormal transformation for the $\{Q_{E_g,1}, Q_{E_g,2}\}$ coordinates to obtain the same matrix as the one given in Ref. [92].

This matrix highlights again the fact that, with no thermal effect, so with $Q_{\Gamma\gamma} = 0$, the 6p levels are not lifted by the crystal field, only a (a_0) global shift of the free transition $6s \rightarrow 6p$ will occur.

In order to complete the calculation, we add the spin degree of freedom with the spin 1/2 basis sets $|\pm\rangle$.

The spin-orbit matrix is

$$H_{\text{SO}} = \frac{A^{\text{SO}}}{2} \begin{pmatrix} |x+\rangle & |y+\rangle & |z+\rangle & |x-\rangle & |y-\rangle & |z-\rangle \\ 0 & -i & 0 & 0 & 0 & 1 \\ i & 0 & 0 & 0 & 0 & -i \\ 0 & 0 & 0 & -1 & i & 0 \\ 0 & 0 & -1 & 0 & i & 0 \\ 0 & 0 & -i & -i & 0 & 0 \\ 1 & i & 0 & 0 & 0 & 0 \end{pmatrix} \quad (\text{A2})$$

And the crystal field matrix takes a simple block form:

$$H_{\text{CF}} = \begin{pmatrix} M_{\text{CF}} & 0 \\ 0 & M_{\text{CF}} \end{pmatrix}$$

3. Hexagonal: D_{3h} , C_{3v}

a. Hexagonal: D_{3h}

The D_{3h} symmetry (as C_2H_6 Eclipsed Ethane), can arise from 5 vacancy in hcp phase, for instance. Its basis vectors are $|E', 1\rangle$, $|E', 2\rangle$, and $|A_2''\rangle = |z\rangle$. The crystal field is, at the lowest order, $V^{(0)}(\mathbf{r}) = a_0^0 Y_0^0 + r^2 a_2 Y_2^0 + \dots$ (with $\hat{Y}_2^0 = 3L_z^2 - L(L+1)$).

And with $[E' \times E'] = A_1' \oplus E'$ we have

$$M_{\text{CF}} = \left(\frac{a_0}{\sqrt{4\pi}} \right) \mathbf{I}_3 + \begin{pmatrix} |E', 1\rangle & |E', 2\rangle & |z\rangle \\ -\frac{\langle r^2 \rangle a_2}{\sqrt{20\pi}} + V_{E'} Q_{E',1} & V_{A_1'} Q_{A_1'} & 0 \\ V_{A_1'} Q_{A_1'} & -\frac{\langle r^2 \rangle a_2}{\sqrt{20\pi}} + V_{E'} Q_{E',2} & 0 \\ 0 & 0 & \frac{2\langle r^2 \rangle a_2}{\sqrt{20\pi}} \end{pmatrix}$$

where $\langle r^2 \rangle = \langle 6p | r^2 | 6p \rangle$ is the square of the size of a Cs atom in its 6p level.

Here the 6p ($l = 1$) degeneracy is partially lifted into two levels by the crystal field and only the spin-orbit will create the triplet structure that is then broadened and modified by the A_1' and E' terms. This symmetry would likely produce a triplet structure.

b. Hexagonal: C_{3v}

The C_{3v} symmetry (as Ammonia NH_3 molecule), can arise in 4 vacancy in an hcp phase. It is very similar

to the D_{3h} symmetry case and can be obtained from it through the substitutions $E' \rightarrow E$, $A_1' \rightarrow A_1$, and $A_2'' \rightarrow A_1$. Therefore, the basis becomes $|E, 1\rangle, |E, 2\rangle, |A_1\rangle = |z\rangle$ and the crystal field that at lowest order is given by: $V^{(0)}(\mathbf{r}) = a_0^0 Y_0^0 + r^2 a_2 Y_2^0 + \dots$. With $[E \times E] = A_1 \oplus E$ we have

$$M_{\text{CF}} = \left(\frac{a_0}{\sqrt{4\pi}} \right) \mathbf{I}_3 + \begin{pmatrix} |E, 1\rangle & |E, 2\rangle & |z\rangle \\ -\frac{\langle r^2 \rangle a_2}{\sqrt{20\pi}} + V_E Q_{E,1} & V_{A_1} Q_{A_1} & 0 \\ V_{A_1} Q_{A_1} & -\frac{\langle r^2 \rangle a_2}{\sqrt{20\pi}} + V_E Q_{E,2} & 0 \\ 0 & 0 & \frac{2\langle r^2 \rangle a_2}{\sqrt{20\pi}} \end{pmatrix}$$

This is identical to the previous case, so this symmetry would likely produce a triplet structure.

$|y\rangle$, and $|A_1\rangle = |z\rangle$. The crystal field is at the lowest order: $V^{(0)}(\mathbf{r}) = a_0^0 Y_0^0 + r^2 a_2 Y_2^0 + \dots$. And with $[E \times E] = A_1 \oplus B_2 \oplus B_1$ we get

4. Tetragonal: C_{4v}

The C_{4v} symmetry (as SF_5Cl or IF_5), can arise in the 10 vacancy case. Its basis is $|E, 1\rangle = |x\rangle$, $|E, 2\rangle =$

$$M_{\text{CF}} = \left(\frac{a_0}{\sqrt{4\pi}} + V_{A_{1g}} Q_{A_{1g}} \right) \mathbf{I}_3 + \begin{pmatrix} |x\rangle & |y\rangle & |z\rangle \\ -\frac{\langle r^2 \rangle a_2}{\sqrt{20\pi}} - V_{B_2} Q_{B_2} & V_{B_1} Q_{B_1} & 0 \\ V_{B_1} Q_{B_1} & -\frac{\langle r^2 \rangle a_2}{\sqrt{20\pi}} + V_{B_2} Q_{B_2} & 0 \\ 0 & 0 & \frac{2\langle r^2 \rangle a_2}{\sqrt{20\pi}} \end{pmatrix}$$

This is very similar to the previous cases, and this symmetry would likely produce a triplet structure.

$|y\rangle$, $|A_1\rangle = |z\rangle$. The crystal field is at the lowest order: $V^{(0)}(\mathbf{r}) = a_0^0 Y_0^0 + r^2 [a_2^0 Y_2^0 + a_2^2 (Y_2^{-2} + Y_2^2)] + \dots$ (with $\hat{Y}_2^{\pm 2} = L_{\pm}^2$) and its matrix takes a diagonal form:

5. Lower symmetry: C_{2v}

The C_{2v} symmetry (as H_2O water molecule), can arise in the 8 vacancy case and has the basis $|B_2\rangle = |x\rangle$, $|B_1\rangle =$

$$M_{\text{CF}} = \left(\frac{a_0}{\sqrt{4\pi}} + V_{A_{1g}} Q_{A_{1g}} \right) \mathbf{I}_3 + \frac{\langle r^2 \rangle}{\sqrt{20\pi}} \begin{pmatrix} |x\rangle & |y\rangle & |z\rangle \\ -a_2^0 + \sqrt{6}a_2^2 & 0 & 0 \\ 0 & -a_2^0 - \sqrt{6}a_2^2 & 0 \\ 0 & 0 & 2a_2^0 \end{pmatrix}$$

Here the $6p$ ($l = 1$) degeneracy is fully lifted in the three levels by the crystal field. The spin-orbit will also shift the levels and the triplet structure will be broadened in a symmetric way by the A_{1g} terms.

Appendix B: Potential curves calculation

We discuss here the Cs-Ar potential for Cs in its $6p$ excited level, the origin of the energy is taken at the $6p$ level in gas phase.

1. Hund's case (a) and (c) curves

Without spin-orbit interaction the Cs(6p)-Ar interaction is diagonal in the basis $|\Pi, \pm\rangle = |L = 1, M = \pm 1\rangle$, $|\Sigma\rangle = |L = 1, M = 0\rangle$ with $V_{\Pi}(R), V_{\Sigma}(R)$ Hund's case (a) potential curves, where R is the Cs-Ar separation.

When adding the spin-orbit $A^{\text{SO}}(R)\mathbf{L}\cdot\mathbf{S}$, the Hamilto-

nian becomes

$$\begin{pmatrix} |\Pi, +\rangle|m_s = -1/2\rangle & |\Sigma\rangle|m_s = 1/2\rangle & |\Pi, +\rangle|m_s = 1/2\rangle \\ V_{\Pi} - \frac{A^{\text{SO}}}{2} & \frac{A^{\text{SO}}}{\sqrt{2}} & 0 \\ \frac{A^{\text{SO}}}{\sqrt{2}} & V_{\Sigma} & 0 \\ 0 & 0 & V_{\Pi} + \frac{A^{\text{SO}}}{2} \end{pmatrix}$$

and the matrix will be identical for the basis with opposite signs for all values of the projection of angular momenta: $|\Pi, -\rangle|m_s = 1/2\rangle, |\Sigma\rangle|m_s = -1/2\rangle, |\Pi, -\rangle|m_s = -1/2\rangle$. The spin-orbit parameter $A^{\text{SO}}(R)$ is not in general constant and deviates from the asymptotic atomic value as shown in Fig. 3 [136]. Taking the eigenvalues leads to the potential curves with spin-orbit $V_{\Pi_{\frac{1}{2}}}, V_{\Pi_{\frac{3}{2}}}, V_{\Sigma_{\frac{1}{2}}}$ with the correspondence:

$$\begin{aligned} V_{\Sigma} &= \frac{1}{3}(2V_{\Pi_{\frac{1}{2}}} - V_{\Pi_{\frac{3}{2}}} + 2V_{\Sigma_{\frac{1}{2}}} + \sqrt{V_{\Pi_{\frac{1}{2}}}^2 + 2V_{\Pi_{\frac{1}{2}}}V_{\Pi_{\frac{3}{2}}} - 2V_{\Pi_{\frac{3}{2}}}^2 - 4V_{\Pi_{\frac{1}{2}}}V_{\Sigma_{\frac{1}{2}}} + 2V_{\Pi_{\frac{3}{2}}}V_{\Sigma_{\frac{1}{2}}} + V_{\Sigma_{\frac{1}{2}}}^2}) \quad (\text{B1}) \\ V_{\Pi} &= \frac{1}{6}(V_{\Pi_{\frac{1}{2}}} + 4V_{\Pi_{\frac{3}{2}}} + V_{\Sigma_{\frac{1}{2}}} - \sqrt{V_{\Pi_{\frac{1}{2}}}^2 + 2V_{\Pi_{\frac{1}{2}}}V_{\Pi_{\frac{3}{2}}} - 2V_{\Pi_{\frac{3}{2}}}^2 - 4V_{\Pi_{\frac{1}{2}}}V_{\Sigma_{\frac{1}{2}}} + 2V_{\Pi_{\frac{3}{2}}}V_{\Sigma_{\frac{1}{2}}} + V_{\Sigma_{\frac{1}{2}}}^2}) \\ A^{\text{SO}} &= \frac{1}{3}(-V_{\Pi_{\frac{1}{2}}} + 2V_{\Pi_{\frac{3}{2}}} - V_{\Sigma_{\frac{1}{2}}} + \sqrt{V_{\Pi_{\frac{1}{2}}}^2 + 2V_{\Pi_{\frac{1}{2}}}V_{\Pi_{\frac{3}{2}}} - 2V_{\Pi_{\frac{3}{2}}}^2 - 4V_{\Pi_{\frac{1}{2}}}V_{\Sigma_{\frac{1}{2}}} + 2V_{\Pi_{\frac{3}{2}}}V_{\Sigma_{\frac{1}{2}}} + V_{\Sigma_{\frac{1}{2}}}^2}) \end{aligned}$$

From this correspondence we have extracted the $V_{\Sigma}(R)$ and $V_{\Pi}(R)$ (and $A^{\text{SO}}(R)$) potential curves from the $V_{\Pi_{\frac{1}{2}}}, V_{\Pi_{\frac{3}{2}}}, V_{\Sigma_{\frac{1}{2}}}$ ones. The calculation is done using the most recent $V_{X^2\Sigma_{1/2}^+}, V_{A\Pi_{1/2}}, V_{A\Pi_{3/2}}, V_{B^2\Sigma_{1/2}^+}$ potentials (in Hund's case (a) notation, but calculated with fine structure included) with spin-orbit interactions from [42] and with a cubic interpolation between points and above 2 nm the long-range part is taken from [41].

2. Cs-Ar sum

Using the primitive cell and lattice vectors, we sum the interaction $\langle L'M'|\hat{V}_{Cs,Ar}(\mathbf{R}_{Cs,Ar})|LM\rangle$ between a Cs atom and all Ar ones. Where $|LM\rangle = |LM\rangle_z$ is quantized along the fixed z axis.

We then use the fixed right-handed frame, right-hand screw counterclockwise rule active interpretation (extrinsic) rotation $z y z$ convention $\mathcal{R}(\alpha, \beta, \gamma) = e^{-i\alpha L_z} e^{-i\beta L_y} e^{-i\gamma L_z}$ [137, 138] such that \mathcal{R} rotates the $|LM\rangle_z$ state to the $|LM\rangle_{\mathcal{R}(z)}$ where the new axis $z' = \mathcal{R}(z)$ is along $\mathbf{R}_{Cs,Ar}$. Thus $\mathbf{L}_{\mathcal{R}(z)} = \mathcal{R}\mathbf{L}_z\mathcal{R}^\dagger$. The calculation is done using active rotation of the state vector and Wigner D-matrix with the convention: ${}_z\langle LM'|\mathcal{R}(\alpha, \beta, \gamma)|LM\rangle_z = D_{M'M}^L(\alpha, \beta, \gamma) = e^{-i\alpha m'} {}_z\langle L'M'|e^{-i\beta L_y}|LM\rangle_z e^{-i\gamma m} = \text{WignerD}[\{L, M', M\}, -\alpha, -\beta, -\gamma]$ (the last notation being adapted for the Mathematica software). Using the spherical coordinate, polar angle θ and azimuthal angle φ , for the vector $\mathbf{R}_{Cs,Ar}$ (from Cs to Ar) we have $\alpha = \varphi, \beta = \theta, \gamma = 0$.

Finally, we find the following matrix for the $\langle L'M'|\hat{V}_{Cs,Ar}(\mathbf{R}_{Cs,Ar})|LM\rangle$ interaction [85, 139]:

$$\begin{pmatrix} |\Pi, -\rangle & |\Sigma\rangle & |\Pi, +\rangle \\ \frac{3V_{\Pi}+V_{\Sigma}+(V_{\Pi}-V_{\Sigma})\cos(2\theta)}{4} & \frac{e^{i\varphi}(V_{\Sigma}-V_{\Pi})\cos\theta\sin\theta}{\sqrt{2}} & \frac{e^{2i\varphi}(V_{\Pi}-V_{\Sigma})\sin^2\theta}{2} \\ \frac{e^{-i\varphi}(V_{\Sigma}-V_{\Pi})\cos\theta\sin\theta}{\sqrt{2}} & V_{\Sigma}\cos^2\theta + V_{\Pi}\sin^2\theta & \frac{e^{i\varphi}(V_{\Pi}-V_{\Sigma})\cos\theta\sin\theta}{\sqrt{2}} \\ \frac{e^{-2i\varphi}(V_{\Pi}-V_{\Sigma})\sin^2\theta}{2} & \frac{e^{-i\varphi}(V_{\Pi}-V_{\Sigma})\cos\theta\sin\theta}{\sqrt{2}} & \frac{3V_{\Pi}+V_{\Sigma}+(V_{\Pi}-V_{\Sigma})\cos(2\theta)}{4} \end{pmatrix} \quad (\text{B2})$$

for a vector \mathbf{R} between the Cs atoms and the Ar

atoms with X, Y, Z cartesian coordinate where $\cos(\theta) =$

$Z/R, e^{\pm i\varphi} \sin(\theta) = (X \pm iY)/R$. Its cartesian form is given by Eq. 2

We then sum over all Ar atoms, using V_Σ and V_Π potentials without spin-orbit interactions in Eq. 2, and after we add a constant spin-orbit interaction that is

$$H_{\text{SO}} = A^{\text{SO}} \begin{pmatrix} |\Pi_- \downarrow\rangle & |\Sigma \downarrow\rangle & |\Pi_+ \downarrow\rangle & |\Pi_- \uparrow\rangle & |\Sigma \uparrow\rangle & |\Pi_+ \uparrow\rangle \\ \frac{1}{2} & 0 & 0 & 0 & 0 & 0 \\ 0 & 0 & 0 & \frac{1}{\sqrt{2}} & 0 & 0 \\ 0 & 0 & -\frac{1}{2} & 0 & \frac{1}{\sqrt{2}} & 0 \\ 0 & \frac{1}{\sqrt{2}} & 0 & -\frac{1}{2} & 0 & 0 \\ 0 & 0 & \frac{1}{\sqrt{2}} & 0 & 0 & 0 \\ 0 & 0 & 0 & 0 & 0 & \frac{1}{2} \end{pmatrix} \quad (\text{B3})$$

Appendix C: Vibrational modes

In order to study the vibronic interactions [140] and the Jahn-Teller effect [93, 101, 113] we use several different mode coordinates. We will detail here all coordinates we used:

- cartesian $\mathbf{R} = \{R_j\}$.
- mass-weighted $\mathbf{Q}^m = \{Q_j^m\} = \mathbf{m}^{1/2}(\mathbf{R} - \mathbf{R}_0)$
- normal modes $\mathbf{Q}^n = \{Q_j^n\} = \mathbf{O}_m^n \dagger \mathbf{Q}^m$ with oscillations ω_n simply noted ω .
- interaction modes $\mathbf{Q}^{\text{int}} = \{Q_j^{\text{int}}\} = \mathbf{V}_r \dagger \mathbf{Q}^n$
- crystal field symmetry adapted interaction modes $\mathbf{Q}^\Gamma = \{Q_{\Gamma\gamma}\} = \mathbf{O}_n^\Gamma \dagger \mathbf{Q}^n$ with oscillations ω^Γ .
- frequency scaled coordinates $\tilde{\mathbf{Q}}^n = \frac{1}{\sqrt{2}} \omega \mathbf{Q}^n$ or $\tilde{\mathbf{Q}}^\Gamma = \frac{1}{\sqrt{2}} \omega^\Gamma \mathbf{Q}^\Gamma$ with unit oscillations frequencies.

and their corresponding momenta conjugate respectively $\hat{\mathbf{P}}, \hat{\mathbf{P}}^m, \hat{\mathbf{P}}^n, \hat{\mathbf{P}}^{\text{int}}, \hat{\mathbf{P}}^\Gamma, \hat{\tilde{\mathbf{P}}}^n, \hat{\tilde{\mathbf{P}}}^\Gamma$.

1. Quantization in the normal modes

We consider the matrix elements $V(\mathbf{R}) = \langle n'l'm' | \hat{V} | nlm \rangle$ for the Cs(6s) and 6p levels.

Neglecting the anharmonic terms, the electron-lattice crystal field $V = V_0 + \nabla_{\mathbf{R}} V^\dagger (\mathbf{R} - \mathbf{R}_0) + \frac{1}{2} (\mathbf{R} - \mathbf{R}_0)^\dagger \nabla_{\mathbf{R}}^2 V (\mathbf{R} - \mathbf{R}_0)$ is numerically evaluated by finite difference: $\nabla_{\mathbf{R}} V_k = \frac{\partial V}{\partial R_k}(\mathbf{R}^0) \approx \frac{V(\mathbf{R}^0 + \delta R_k) - V(\mathbf{R}^0 - \delta R_k)}{2\delta R_k}$ and $\nabla_{\mathbf{R}}^2 V_{kl} = \frac{\partial^2 V}{\partial R_k \partial R_l}(\mathbf{R}^0) \approx \frac{\frac{\partial V}{\partial R_l}(\mathbf{R}^0 + \delta R_k) - \frac{\partial V}{\partial R_l}(\mathbf{R}^0 - \delta R_k)}{2\delta R_k}$

Where we have used standard row vector $\mathbf{R}^\dagger = (R_1, R_2, \dots)$, $\nabla_{\mathbf{R}} V^\dagger = (\frac{\partial V}{\partial R_1}, \frac{\partial V}{\partial R_2}, \dots)$ (\dagger being the Hermitian adjoint, that is the conjugate transpose) and matrix $\nabla_{\mathbf{R}}^2 V$ notations.

In order to treat all kinetic energy terms $\frac{\hat{P}_k^2}{2m_k}$, ($\hat{P}_k = -i\hbar \frac{\partial}{\partial R_k}$ being the quantized momentum conjugate coordinate) in a similar manner, we use the $3(N-n+1)$ mass-weighted Cartesian coordinates $Q_j^m = (R_j - R_{0j})\sqrt{m_j}$ where m_j is the mass of the atom on which the j^{th} coordinate resides. We define the diagonal mass matrix \mathbf{m} with $m_{jj} = m_j$ and $\mathbf{Q}^{m\dagger} = (Q_1^m, Q_2^m, \dots)$, $\nabla_{\mathbf{Q}^m} \dagger = (\frac{\partial V}{\partial Q_1^m}, \frac{\partial V}{\partial Q_2^m}, \dots)$.

So the nuclear Hamiltonian in a Born-Oppenheimer approximation $\hat{H} = \frac{1}{2} \hat{\mathbf{P}}^\dagger \mathbf{m}^{-1} \hat{\mathbf{P}} + V_0 + \nabla_{\mathbf{R}} V^\dagger (\mathbf{R} - \mathbf{R}_0) + \frac{1}{2} (\mathbf{R} - \mathbf{R}_0)^\dagger \nabla_{\mathbf{R}}^2 V (\mathbf{R} - \mathbf{R}_0)$ becomes simply $\hat{H} = \frac{1}{2} \hat{\mathbf{P}}_{\mathbf{Q}^m}^\dagger \hat{\mathbf{P}}_{\mathbf{Q}^m} + V_0 + \nabla_{\mathbf{Q}^m} V^\dagger \mathbf{Q}^m + \frac{1}{2} \mathbf{Q}^{m\dagger} \nabla_{\mathbf{Q}^m}^2 V \mathbf{Q}^m$, where we have used $\hat{\mathbf{P}}_{\mathbf{Q}^m} = \mathbf{m}^{-1/2} \hat{\mathbf{P}}$ vector notation for the momentum conjugate with the \mathbf{Q}^m coordinates, that verifies the canonical commutation relation $[\mathbf{Q}^m, \hat{\mathbf{P}}_{\mathbf{Q}^m}] = [\mathbf{R}, \hat{\mathbf{P}}] = \mathbf{R} \hat{\mathbf{P}}^\dagger - \hat{\mathbf{P}} \mathbf{R}^\dagger = i\hbar \mathbf{1}$.

The eigendecomposition of the Hessian matrix $\nabla_{\mathbf{Q}^m}^2 V = \mathbf{O}_m^n \omega^2 \mathbf{O}_m^n \dagger$ creates the the normal vibrational modes $\mathbf{Q}^n = \mathbf{O}_m^n \dagger \mathbf{Q}^m$ with \mathbf{O}_m^n the change-of-basis orthonormal matrix and ω a diagonal matrix with the k -th element being the (mass scaled) oscillation angular frequency ω_k . The Hamiltonian is thus written as

$$\hat{H} = \frac{1}{2} \hat{\mathbf{P}}_{\mathbf{Q}^n}^\dagger \hat{\mathbf{P}}_{\mathbf{Q}^n} + V_0 + \nabla_{\mathbf{Q}^n} V^\dagger \mathbf{Q}^n + \frac{1}{2} \mathbf{Q}^{n\dagger} \omega^2 \mathbf{Q}^n \quad (\text{C1})$$

$$= \sum_k -\hbar^2 \frac{\partial^2}{\partial^2 Q_k^n} + V_0 + (\nabla_{\mathbf{Q}^n} V^*)_k Q_k^n + \frac{1}{2} \omega_k^2 Q_k^{n2}$$

with $\nabla_{\mathbf{Q}^n} V = \mathbf{O}_m^n \dagger \nabla_{\mathbf{Q}^m} V$ and $\hat{\mathbf{P}}_{\mathbf{Q}^n} = \mathbf{O}_m^n \dagger \hat{\mathbf{P}}_{\mathbf{Q}^m}$ is the conjugate momentum with $[\mathbf{Q}^n, \hat{\mathbf{P}}_{\mathbf{Q}^n}] = i\hbar \mathbf{1}$.

2. First order: crystal field coefficient

We will now use the decomposition (C1) for $V(\mathbf{R}) = \langle 6pm' | \hat{V} | 6pm \rangle$.

a. *Crystal field coefficients*

In order to determine the (real) crystal fields coefficients V_Γ , that are the $(\nabla_{\mathbf{Q}^\Gamma} V^\dagger)_{m'm} = \langle m' | \frac{\partial V}{\partial Q_{\Gamma\gamma}} | m \rangle$ coefficients present in the 3×3 crystal field matrix M_{CF} , we restrict ourselves to only the first order series in nuclear coordinates. Thus $V = \langle 6pm' | \hat{V} | 6pm \rangle$ contains only $(V_0)_{m'm} + (\nabla_{\mathbf{Q}^\Gamma} V^\dagger)_{m'm} \mathbf{Q}^\Gamma$ type of terms. We will put the $(\nabla_{\mathbf{Q}^\Gamma} V^\dagger)_{m'm}$ values in a $3 \times 3 = 9$ rows matrix, with each row linked to a given m', m .

The first order potential can be calculated using the normal mode basis \mathbf{Q}^Γ or expressed in the expected M_{CF} crystal field ones. Equalizing the two expressions leads to the equation $\nabla_{\mathbf{Q}^\Gamma} V^\dagger \mathbf{Q}^\Gamma = \nabla_{\mathbf{Q}^\Gamma} V^\dagger \mathbf{Q}^\Gamma$.

Without knowing the orthonormal transformation, $\mathbf{Q}^\Gamma = \mathbf{O}_n^{\Gamma\dagger} \mathbf{Q}^\Gamma$ that links the crystal field symmetry adapted interaction mode coordinates $Q_{\Gamma\gamma}$ to the normal mode coordinates Q_k^n , the use of the fact that the transformation is orthonormal leads to a 9×9 matrix equation

$$\nabla_{\mathbf{Q}^\Gamma} V^\dagger \nabla_{\mathbf{Q}^\Gamma} V = \nabla_{\mathbf{Q}^\Gamma} V^\dagger \nabla_{\mathbf{Q}^\Gamma} V \quad (\text{C2})$$

that, when solved, gives the crystal field coefficients $\nabla_{\mathbf{Q}^\Gamma} V$.

b. *Interaction mode coordinates*

In order to perform Monte Carlo simulations, it might be important to know how the crystal field symmetry adapted interaction mode coordinates \mathbf{Q}^Γ can be calculated.

They can be found using the singular value decomposition of the 9 rows matrix $\nabla_{\mathbf{Q}^\Gamma} V^\dagger = \mathbf{U} \mathbf{W} \mathbf{V}^\dagger$ of rank r (the matrix \mathbf{V} not being confused with the potential V). Equation $\nabla_{\mathbf{Q}^\Gamma} V^\dagger \mathbf{Q}^\Gamma = \nabla_{\mathbf{Q}^\Gamma} V^\dagger \mathbf{Q}^\Gamma$ leads to $\nabla_{\mathbf{Q}^\Gamma} V^\dagger \mathbf{Q}^\Gamma = (\mathbf{U} \mathbf{W})(\mathbf{V}^\dagger \mathbf{Q}^\Gamma)$. We cannot simply equalize $\nabla_{\mathbf{Q}^\Gamma} V^\dagger$ with $\mathbf{U} \mathbf{W}$ and \mathbf{Q}^Γ with $\mathbf{V}^\dagger \mathbf{Q}^\Gamma$ because $\mathbf{Q}^{\text{int}} = (\mathbf{V}^\dagger \mathbf{Q}^\Gamma)$ is only one choice for the interaction mode coordinates, that is not necessarily the same basis (for instance not in the same order, same sign, ...) as the $\mathbf{Q}^\Gamma = \{Q_{\Gamma\gamma}\}$ used to determine from symmetry consideration the crystal field matrix M_{CF} . However, using the only useful first r rows of the r blocks matrix restriction (noted with index r) of $(\mathbf{W}_r)^{-1} \mathbf{U}_r^\dagger (\nabla_{\mathbf{Q}^\Gamma} V^\dagger \cdot \mathbf{Q}^\Gamma) = \mathbf{Q}^{\text{int}} = (\mathbf{V}_r^\dagger \mathbf{Q}^\Gamma)$ leads to the transformation $\mathbf{Q}^\Gamma = \mathbf{O}_n^{\Gamma\dagger} \mathbf{Q}^\Gamma$. Where, for simplicity, we have kept the same notation \mathbf{Q}^Γ or \mathbf{Q}^{int} for the first r interaction modes coordinates than for the $3N$ ones.

The important fact is that the diagonal matrix \mathbf{W} has only r non-zero singular values on the diagonal (so \mathbf{W}_r is square diagonal of size r), and thus we will often be interested only in the r relevant (r first) interaction modes coordinates.

With these new coordinates it turns out that the $r \times r$ matrix $(\omega_\Gamma)^2 = \mathbf{O}_n^{\Gamma\dagger} \omega^2 \mathbf{O}_n^\Gamma$ matrix is diagonal. We thus

have

$$\langle 6s | \hat{V} | 6s \rangle = V_0 + \frac{1}{2} \mathbf{Q}^{\Gamma\dagger} (\omega^\Gamma)^2 \mathbf{Q}^\Gamma = V_0 + \sum_{\Gamma\gamma=1}^r \frac{1}{2} \omega_{\Gamma\gamma}^2 Q_{\Gamma\gamma}^2 \quad (\text{C3})$$

Once again, we see the advantage of using the interaction mode coordinates to reduce drastically the number of modes to be calculated. The Monte Carlo simulation becomes very simple because we have to calculate only few ($r \leq 9$) interaction mode coordinates, such as $\mathbf{Q}^\Gamma = \{Q_{A,1}, Q_{E,1}, Q_{E,2}, Q_{T,1}, Q_{T,2}, Q_{T,3}\}$ to be compared to $\sim 3N$ modes in standard molecular dynamic simulation (almost 10000 in our case for the ~ 3000 movable atoms).

3. Frequency scaled coordinates

Following [91, 92], it might be interesting to use the oscillation frequency scaled coordinates $\tilde{\mathbf{Q}}^n = \frac{1}{\sqrt{2}} \omega \mathbf{Q}^n$ and $\tilde{\mathbf{Q}}^\Gamma = \frac{1}{\sqrt{2}} \omega^\Gamma \mathbf{Q}^\Gamma$ such that Eq. (C3) become

$$\begin{aligned} \langle 6s | \hat{V} | 6s \rangle &= V_0 + \tilde{\mathbf{Q}}^{n\dagger} \tilde{\mathbf{Q}}^n = V_0 + \sum_k \tilde{Q}_k^{n2} \\ &= V_0 + \sum_{\Gamma\gamma=1}^r \tilde{Q}_{\Gamma\gamma}^2 \end{aligned}$$

This form is interesting, because in a pure classical molecular dynamical simulation, the Boltzmann statistics indicates that $\tilde{\mathbf{Q}}^n$ follows a multivariate normal distribution $\propto e^{-\frac{1}{2} \tilde{\mathbf{Q}}^{n\dagger} \tilde{\Sigma}^{-1} \tilde{\mathbf{Q}}^n}$ with a variance $\tilde{\Sigma}^n = \frac{1}{2} k_B T \mathbf{I}$. That way the interaction mode coordinate vector $\tilde{\mathbf{Q}}^\Gamma = \mathbf{O}_n^{\Gamma\dagger} \tilde{\mathbf{Q}}^n$ follows a multivariate normal distribution with a variance that is also diagonal: $\tilde{\Sigma}^\Gamma = \mathbf{O}_n^{\Gamma\dagger} \tilde{\Sigma}^n \mathbf{O}_n^\Gamma = \frac{1}{2} k_B T \mathbf{I}$. Thus, in a standard classical Monte Carlo simulation at temperature T , each $\frac{\tilde{Q}_{\Gamma\gamma}}{\sqrt{k_B T/2}}$ coordinate has the same distribution: a standard unit normal (Gaussian).

It is even possible to keep the normalized coordinate in a classical simulation that includes the temperature scale T' by having $\tilde{\mathbf{Q}}^n$ following a multivariate normal distribution with a new diagonal variance $\tilde{\Sigma}^{n'}$ with diagonal element given by $\frac{1}{2} k_B T' (\omega_k)$ according to Eq. (6), namely $\frac{\tilde{Q}_k^n}{\sqrt{k_B T' (\omega_k)/2}}$. In this case, $\tilde{\mathbf{Q}}^\Gamma$ has simply to be chosen with a Gaussian variance $\tilde{\Sigma}^{\Gamma'} = \mathbf{O}_n^{\Gamma\dagger} \tilde{\Sigma}^{n'} \mathbf{O}_n^\Gamma$. Another strategy, that leads to the same final result, is to keep the unit normal distribution for $\frac{\tilde{Q}_k^n}{\sqrt{k_B T/2}}$ but change each ω_k into ω'_k such that $\omega_k'^2/T = \omega_k^2/T' (\omega_k)$.

So, as used in Ref. [91, 92], such frequency scaled coordinates are useful in classical simulations because the oscillations frequencies ω^Γ (or the scaled ones ω'^Γ) of the modes are not needed, if we include them in the definition of new crystal field parameters $\tilde{V}_\Gamma = \sqrt{2} V_\Gamma / \omega_\Gamma$. Then all terms in the interaction matrix can be written using

$V_\Gamma Q_{\Gamma\gamma} = \tilde{V}_\Gamma \tilde{Q}_{\Gamma\gamma}$ with now Eq. (9) becoming Eq. (10) that is

$$A(E) \propto \int \sum_{i=1}^6 \delta[E - X_i(\tilde{Q}^\Gamma)] e^{-\sum_{\Gamma\gamma} \tilde{Q}_{\Gamma\gamma}^2/k_B T} d\tilde{Q}^\Gamma \quad (\text{C4})$$

with the $\frac{\tilde{Q}_{\Gamma\gamma}}{\sqrt{k_B T/2}}$ coordinates having a standard unit normal (Gaussian) distribution.

To illustrate this, we mention that the values given in Ref. [18] for the crystal field in Table I are

$$\begin{aligned} A &= \frac{\sqrt{k_B T/2}}{A^{SO}} \tilde{V}_{A_1} = \frac{\sqrt{k_B T/2}}{A^{SO}} \frac{\omega_\Gamma}{\omega_{A_1}} V_{A_1} = 0.294, \\ B &= \frac{\sqrt{k_B T/3}}{A^{SO}} \tilde{V}_E = \frac{\sqrt{k_B T/3}}{A^{SO}} \frac{\omega_\Gamma}{\omega_E} V_E = 0.6, \\ C &= \frac{\sqrt{k_B T/4}}{A^{SO}} \tilde{V}_{T_2} = \frac{\sqrt{k_B T/4}}{A^{SO}} \frac{\omega_\Gamma}{\omega_{T_2}} V_{T_2} = 0.2. \end{aligned}$$

Indeed the linear part of the potential is

$$V_{\Gamma\gamma} Q_{\Gamma\gamma} = A^{SO} \left(\frac{\sqrt{k_B T/x_\Gamma}}{A^{SO}} \frac{\omega_\Gamma}{\omega_\Gamma} V_{\Gamma\gamma} \right) \left(\frac{1}{\sqrt{k_B T/x_\Gamma}} \frac{\omega_\Gamma}{\sqrt{2}} Q_{\Gamma\gamma} \right)$$

(x_Γ is 2 for the case of $\Gamma = A_1$, 3 for E_2 and 4 for T_2 [92]).

In the above notation, the ground state potential reduces to $\sum_{\Gamma\gamma} \frac{1}{2} \omega_\Gamma^2 Q_{\Gamma\gamma}^2 = \sum_{\Gamma\gamma} \tilde{Q}_{\Gamma\gamma}^2$.

For the quantized simulation, this frequency scaled coordinates procedure does not work anymore because the quantized energy levels are intrinsically linked to the frequencies, that thus cannot be simply scaled. We could think of using the frequency scaled coordinates with unity frequencies such that all modes look similar and the number of different modes would appear to matter less. However this approach is futile because, the kinetic energy of the lattice (from Eq. (C1)) would not be diagonal in the momenta conjugate to the scaled interaction mode anymore, as already has been noticed in Ref. [91]. This is not important in the classical Franck-Condon Mulliken approximation where the kinetic energy plays no role because there, we only need to find the positions that are determined by the Boltzmann distribution involving only the potential energy. It, however, becomes crucial for quantized energies, such as in the reflection approximation.

4. Coordinate distribution

Let us mention that at $T = 0\text{K}$ each normal mode $|\Psi_i(\mathbf{Q}_k)|^2$ distribution is gaussian (ground state of the harmonic oscillator) and so the multivariate normal distribution $\propto e^{-\frac{1}{2} \mathbf{Q}^n \boldsymbol{\Sigma}^{-1} \mathbf{Q}^n}$ of the \mathbf{Q}^n normal modes is transformed in a multivariate normal distribution with a variance $\boldsymbol{\Sigma}^\Gamma = \mathbf{O}_n^\Gamma \boldsymbol{\Sigma}^n \mathbf{O}_n^\Gamma$ for the interaction mode. It turns out that the marginal distribution for the 6 mode coordinates is indeed a variance that is diagonal. This is a consequence of the fact that the projection on the 6 mode coordinates on the ground state Hessian matrix is diagonal with the frequencies ω^Γ given in Table

I. Together with the fact that the first order approximation is quite accurate for the excited state interaction this leads to the fact that the $T = 0\text{K}$ spectra can be calculated in a pure crystal field model with only 6 coordinates simply using frequencies ω^Γ to determine the gaussian Q^Γ coordinates using temperature scaling or the ground state wavefunction of the $\frac{1}{2} \omega_\Gamma^2 Q_{\Gamma\gamma}^2$ harmonic oscillator. The result for $T = 0\text{K}$ gives the same spectra as the one in Fig. 9. Indeed at $T = 0\text{K}$ each E_i is constant and is the zero point energy the i -th modes. By offsetting to this value, we have at $T = 0\text{K}$, $E_i = 0$ and so the reflexion approximation is $A(E) \propto \sum_{i=1}^6 P_i \int |\Psi_i(\mathbf{Q})|^2 \delta[E - (V_{\text{Cs}(6p)-\text{Ar}}(\mathbf{Q}) - E_i)] d\mathbf{Q}$ which can be compared to the formula (11).

Appendix D: Semi-classical approximations

To study laser excitation of the (6s) cesium atom toward the 6p manifold we start (thanks to the Beer-Lambert-Bouguer's law) by using the fact that the spectral density optical absorption coefficient $A(E)$ for a photon of energy E , is given by the sum over all initial vibronic levels $|i\rangle$, populated with probability P_i with wavefunction $\Psi_i(\mathbf{Q})$ of energy E_i , towards all possible final ones $\Psi_f(\mathbf{Q})$ of energy E_f :

$$A(E) \propto \sum_{if} P_i \delta[E - (E_f - E_i)] \left| \int \Psi_f^\dagger(\mathbf{Q}) d_{if}(\mathbf{Q}) \Psi_i(\mathbf{Q}) d\mathbf{Q} \right|^2 \quad (\text{D1})$$

Thus $A(E)dE$ is the absorption coefficient for a photon in the energy band $E, E + dE$.

1. Semi-classical Franck-Condon approximation

In our case, the variation of the dipole transition strength from X to Σ or Π states is on the order of 10% [41]. So we can reasonably consider variation of the dipole $d_{if}(\mathbf{Q})$ with the internuclear distances \mathbf{Q} as negligible (this is the "Condon" approximation [79]). If needed, a better approximation would be the Herzberg-Teller centroid one with d_{if} taken at the point $\bar{\mathbf{Q}}$, which cancels the first order evolution in \mathbf{Q} . In the following, for simplicity we will assume $d_{if}(\mathbf{Q}) \approx d_{if}(\bar{\mathbf{Q}})$ to be constant (it is simply the 6s to 6p dipole transition and can thus be left out of the equation). Furthermore, we can also justify an isotropic nature of the dipole in our case because our sample's poly-crystalline structure leads to random orientations of the crystal axes.

In our case, after laser excitation of the Cs(6s) atom from its equilibrium position, the Cs(6p) atom is far from being in its equilibrium position and the excited electron potentials are mostly linear and not quadratic. Thus the motional excited states will be states with large vibrational quantum numbers or even quasi continuum one, which, according to the Bohr correspondence principle,

can be treated as approximately classical. Thus, following [79] we can assume transitions near the classical turning points and for the sum over f we can replace E_f in the delta-function by a mean value independent of f that is the electron excited (6p) potential energy curve $V_e(\mathbf{Q})$ so:

$$A(E) \propto \sum_i P_i \int \delta[E - (V_e(\mathbf{Q}) - E_i)] |\Psi_i(\mathbf{Q})|^2 d\mathbf{Q} \quad (\text{D2})$$

This expression is also called the reflection approximation [80].

If many initial states (vibrational for instance) i are involved, it is convenient to use a mean-value approximation using for the ground state energies, the potential energy $V_g(\mathbf{Q})$ leading to the so-called semiclassical Franck-Condon formula

$$A(E) \propto \int \delta[E - (V_e(\mathbf{Q}) - V_g(\mathbf{Q}))] P_g(\mathbf{Q}) d\mathbf{Q} \quad (\text{D3})$$

with $P_g(\mathbf{Q}) = \sum_i P_i |\Psi_i(\mathbf{Q})|^2$ is the quantum-statistical mechanical probability distribution. In the case where $P_g(\mathbf{Q})$ is given by classical statistics, the expression becomes the standard classical Franck-Condon formula [79].

2. Semiclassical transition in energy or in phase space

It is useful to present the spectral density transition probability $P(E_0)$, for a transition energy E_0 given by Eq. (D1), in a state picture

$$P(E_0) = \sum_{f,i} P_i \left| \langle \Psi_f | \hat{d} | \Psi_i \rangle \right|^2 \delta(E_0 - (E_f - E_i)) \quad (\text{D4})$$

because $2\pi P(E_0)/\hbar$ can now be interpreted as a rate given by Fermi's Golden rule [100, 141, 142].

This can be written simply as (in the Condon or centroid approximation where we forget about d^2 from now on), for a pure state ($P_i = 1$ to simplify the notation) as

$$\begin{aligned} P(E_0) &= \sum_{f,i} \langle \psi_f | \psi_i \rangle \langle \psi_i | \psi_f \rangle \langle \psi_f | \delta(E_0 - (\hat{H}_f - E_i)) | \psi_f \rangle \\ &= \sum_{f,i} \langle \psi_f | \psi_i \rangle \langle \psi_i | \sum_{f'} |\psi_{f'}\rangle \langle \psi_{f'} | \delta(E_0 - (\hat{H}_f - E_i)) | \psi_f \rangle \\ &= \sum_f \langle \psi_f | \left(\sum_i |\psi_i\rangle \langle \psi_i | \delta(E_0 - (\hat{H}_f - E_i)) \right) | \psi_f \rangle \\ &= \text{Tr} \left[\sum_i |\psi_i\rangle \langle \psi_i | \delta(E_0 - (\hat{H}_f - E_i)) \right] \\ &= \text{Tr} [\hat{\rho}_i \delta(E_0 - (\hat{H}_f - E_i))] \\ &= \langle \delta(E_0 - (\hat{H}_f - E_i)) \rangle \\ &= \langle \delta(E_0 - (\hat{V}_f - \hat{V}_i) - (\hat{H}_i - E_i)) \rangle \end{aligned}$$

where $\hat{H}_i = \sum_k \hat{P}_k^2 / (2m_k) + V_i(\hat{\mathbf{Q}})$ and $\hat{H}_f = \sum_k \hat{P}_k^2 / (2m_k) + V_f(\hat{\mathbf{Q}})$ are the Hamilton operators respectively for the initial and final electronic state

and $\hat{\rho}_i = \sum_i |\Psi_i\rangle \langle \Psi_i|$ is the density matrix operators for the initial state. The formula can also be written, in the case of a pure state as $P(E_0) = \frac{1}{2\pi\hbar} \int dt e^{i(E_0 - \hat{E}_i)t/\hbar} \langle \Psi_i | \Psi_i(t) \rangle$ where $|\Psi_i(t)\rangle = e^{-i\hat{H}_f t/\hbar} |\Psi_i\rangle$. This time (and Fourier transform) picture opens another way to treat the transition using the (wave packet) time evolution of the system to find $|\psi(t)\rangle$ [116, 118, 119, 143, 144].

One of the best approximations for the formula is clearly to use $\hat{H}_i - E_i$ as a perturbation, especially when projected on $|\psi_i\rangle$ because $\langle \psi_i | \hat{H}_i - E_i | \psi_i \rangle = 0$. Therefore the simplest natural approximation is the zero-order ones for a d dimensional space:

$$\begin{aligned} P(E_0) &= \langle \delta(E_0 - (\hat{V}_f - \hat{V}_i)) \rangle \\ &= (2\pi\hbar)^{-d} \sum_i \int d\mathbf{Q} |\psi_i(\mathbf{Q})|^2 \delta((E - V_f(\mathbf{Q}) + V_i(\mathbf{Q}))) \end{aligned} \quad (\text{D5})$$

This is exactly the same as the formula (D3). But, note that this derivation differs considerably from the previous traditional derivation despite the final results being the same. For instance, it gives a very clear physical understanding that the reflection approximation of Eq. (5) is reproduced under the extra approximation of $\delta(E - (H_{f,cl} - H_{i,cl}))$ replaced by $\delta(E - (V_f(\mathbf{Q}) - E_i))$.

A very similar derivation has been done by moving to the Wigner representation of quantum mechanics [117, 118, 145–148] where the exact formula for $P(E_0)$ becomes, in d dimension, simply $P(E_0) = (2\pi\hbar)^{-d} \int d\mathbf{P} d\mathbf{Q} \rho_{iW} \delta(E_0 - (\hat{H}_f - E_i))_W$ where $_W$ designating the Wigner transform. The leading order in \hbar is simply the semi-classical limit with $\hat{H}_{f,i}$ replaced by their classical counterpart $H_{f,i} = \sum_k \hat{P}_k / (2m_k) + V_{f,i}(\mathbf{Q})$ and ρ_{iW} replaced by the classical phase space density $\rho_{cl} \propto e^{-H_{cl}/k_B T}$. It is obviously slightly better to keep the true Wigner function ρ_{iW} (also because it is known analytically for the harmonic potential case) to have [121]: $P(E) = (2\pi\hbar)^{-d} \int d\mathbf{P} d\mathbf{Q} \rho_{iW} \delta(E - (H_{f,cl} - H_{i,cl}))$. This is again the same formula (D3) if using the fact that integration of the Wigner function over \mathbf{P} gives exactly the wavefunction probability distribution $|\psi_i(\mathbf{Q})|^2$ [145]. This derivation has the advantage of justifying the use of the true quantum (or Wigner) phase-space initial distribution and not the classical one. Thus the probability P_i has to be chosen accordingly to the actual quantum distribution.

Another advantage of this semi-classical phase space picture is that it allows for systematic series expansion, typically in power of \hbar order corrections [80, 117–123]. Finally, the method can be generalized for non-radiative transitions, such as surface hopping non-adiabatic effects or electron transfer with instanton theory or other non Born–Oppenheimer effects [121, 149–152].

Appendix E: Third order many-body term

We will detail some calculations to determine the effective two-body potential from the sum of the third-order terms. For this, we will first derive the general expression for the third-order terms and calculate it for the long-range dipolar case and in a simple two-level approximation. This will allow us to create a mean field of long-range third-order terms that we compare to the long-range part of the two-body case. We finally extend this comparison for all internuclear distances to produce an effective two-body potential that includes the third-order effect.

1. Perturbation theory up to third order

The energy shift ΔE of the energy E of the full system of a given atom A (Cs in our case) in a given state $|lm\rangle$ within the crystal formed by many other atoms (Ar in our case) can be estimated by the perturbation theory from

$$E_{123}^{(3)} = \sum_{\sigma \in S_3, m_1, m_2, m_3} \frac{\langle 0_{\sigma(1)} 0_{\sigma(2)} | V_{\sigma(1)\sigma(2)} | m_{\sigma(1)} m_{\sigma(2)} \rangle \langle m_{\sigma(2)} 0_{\sigma(3)} | V_{\sigma(2)\sigma(3)} | 0_{\sigma(2)} m_{\sigma(3)} \rangle \langle m_{\sigma(3)} m_{\sigma(1)} | V_{\sigma(3)\sigma(1)} | 0_{\sigma(3)} 0_{\sigma(1)} \rangle}{(\Delta_{m_{\sigma(1)}}(\sigma(1)) + \Delta_{m_{\sigma(2)}}(\sigma(2)))(\Delta_{m_{\sigma(1)}}(\sigma(1)) + \Delta_{m_{\sigma(3)}}(\sigma(3)))} \quad (\text{E1})$$

2. dipole dipole dipole long-range interaction

We will calculate these terms in the dipolar long-range interaction case.

We thus assume a dipolar type of interaction (with a fixed quantization axis named z). For two atoms labeled 1 and 2 with internuclear separation $\mathbf{R}_{12} = R_{12}\mathbf{e}_{12}$ where \mathbf{e}_{12} is a unit vector, the dipole-dipole interaction is $V_{12} = \frac{e^2}{4\pi\epsilon_0 R_{12}^3} [\mathbf{r}(1) \cdot \mathbf{r}(2) - 3(\mathbf{r}(1) \cdot \mathbf{e}_{12})(\mathbf{r}(2) \cdot \mathbf{e}_{12})] = \frac{e^2}{4\pi\epsilon_0 R_{12}^3} \mathbf{r}(1) \cdot (1 - 3\mathbf{e}_{12}\mathbf{e}_{12}) \cdot \mathbf{r}(2)$.

That can be written using the irreducible tensors notation. $r_q = r\sqrt{\frac{4\pi}{3}}Y_{1q}(\mathbf{r})$, as

$$V_{12} = -\frac{e^2}{4\pi\epsilon_0 R^3} \sqrt{6}C(\mathbf{e}_{12}) \cdot \{\mathbf{r}(1) \otimes \mathbf{r}(2)\}_2 \quad \text{where} \\ C_M(\mathbf{e}_{12}) = \sqrt{\frac{4\pi}{5}}Y_{2M}(\mathbf{e}_{12}) \quad \text{and} \quad \{\mathbf{r}(1) \otimes \mathbf{r}(2)\}_{2M} = \sum_{q,q'} C_{1q_1q'}^{2M} r_{q_1}(1)r_{q'}(2). \quad \text{So}$$

$$V_{12} = -\frac{\sqrt{6}e^2}{4\pi\epsilon_0 R_{12}^3} \sum_{M, q_1, q_2} (-1)^M C_{-M}(\mathbf{e}_{12}) C_{1q_1 1q_2}^{2M} r_{q_1}(1)r_{q_2}(2)$$

We will often use atomic units where $\frac{e^2}{4\pi\epsilon_0} = 1$. This can be simply realized by changing $r(i)$ in $r(i)\sqrt{\frac{e^2}{4\pi\epsilon_0}}$.

the full hamiltonian energy $H = \sum_i H_0(i) + \frac{1}{2} \sum_{i \neq j} V_{ij}$ where $H_0(i)$ is the single i^{th} atom hamiltonian and $V_{ij}(\mathbf{r}_i, \mathbf{r}_j, \mathbf{R}_i, \mathbf{R}_j)$ contains all electrostatic interactions between the i^{th} atom and the j^{th} with electron coordinates $\mathbf{r}_i, \mathbf{r}_j$ and nuclear ones $\mathbf{R}_i, \mathbf{R}_j$.

We note the eigenstates of the single atom Hamiltonian $H_0(i)$ as $|0_i\rangle$ for the initial (not necessarily the ground state in the Cs case) state of atom i of energy E_{0_i} and $|m_i\rangle$ the other states of energy E_{m_i} .

We calculate the energy shift $\Delta E(\mathbf{R})$ that only depends on the nuclear coordinates \mathbf{R} by perturbation theory. Up to the third-order, the full crystal energy is $\frac{1}{2} \sum_{AB} E_{AB}^{(2)} + \frac{1}{6} \sum_{ABC} E_{ABC}^{(3)} = \sum_{A<B} E_{AB}^{(2)} + \sum_{A<B<C} E_{ABC}^{(3)}$. The first order is zero and the second order leads to a shift depending on atom A given by $\sum_B E_{AB}^{(2)}$ where $E_{12}^{(2)} = \sum_{m_1, m_2} -\frac{|\langle 0_1 0_2 | V_{12} | m_1 m_2 \rangle|^2}{\Delta_{m_1}(1) + \Delta_{m_2}(2)}$ with $\Delta_{m_i}(i) = E_{m_i} - E_{0_i}$.

The third-order perturbation theory terms depend on three atoms A, B, and C. Using the symmetry group S_3 of permutations of the 3 atoms A=1, B=2, C=3, and using $V_{ij} = V_{ji}$, $E_{ABC}^{(3)} = E_{123}^{(3)}$ is the sum of six terms (see [153] (7b)):

a. Two level approximation

One of the simplest approximations is to consider a single effective atomic energy transition, in the pure case, a $S \leftrightarrow P$ transition for each atom (energy difference $E_{SP}(\text{Cs})$ for Cs and $E_{SP}(\text{Ar})$ for Ar). In our case, all Ar atoms are in the ground state S , but the Cs can be either in ground S or in excited state P . Therefore, S or P degeneracy means that, in Eq. (E1), all energy terms are independent of m_i . We write $\Delta_{m_i}(\sigma(i)) = \Delta(\sigma(i))$ that can be factorized out of the sum in Eq. (E1).

Using Cs as atom 1 and Ar for 2 and 3, we have for $i = 2, 3$ $|0_i\rangle = |l = 0m = 0\rangle$ and $|m_i\rangle = |l = 1m = m_i\rangle$ states.

We then follow the elegant derivation done in ref. [154]. We first look on terms depending on m_2 so for i label for which $\sigma(i) = 2$, in Eq. (E1) we have terms $\langle 0_2 | V(j2) | m_2 \rangle$ and $\langle m_2 | V(2k) | 0_2 \rangle$. So using the Wigner-Eckart theorem $\langle l'm' | r_2^{(q)} | lm \rangle = \frac{C_{lm_1q}^{l'm'}}{\sqrt{2^{l'+1}}} \langle l' || r_2 || l \rangle$ the $\sum_{m_2} \langle 0_2 | V(j2) | m_2 \rangle \dots \langle m_2 | V(2k) | 0_2 \rangle$ sum (the \dots are simply here to indicate that the terms are not necessary neighbors in Eq. (E1)) contains $\sum_{m_2} \langle 0_2 | r_{q_2}(2) | m_2 \rangle \dots \langle m_2 | r_{q'_2}(2) | 0_2 \rangle = -\sum_{m_2} C_{1m_2 1q_2}^{00} \dots \frac{C_{001q'_2}^{001m_2}}{\sqrt{3}} \langle 1 || r(2) || 0 \rangle^2$, where we have used

$\langle 0||r(2)||1\rangle = -\langle 1||r(2)||0\rangle$. Then, $\sum_{m_2=-1}^{m_2=1}$ leads to $\frac{\langle 1||r(2)||0\rangle^2}{3}\delta_{q_2,-q'_2}(-1)^{q_2}$. Similar results arise for atoms 3, for j label for which $\sigma(j) = 3$.

b. Interaction between ground state atoms

If the Cs atom is in its ground state, the levels are $|0_1\rangle = |l=0 m=0\rangle$ and $|m_1\rangle = |l=1 m_1\rangle$.

The second order leads to

$$E_{12}^{(2)} = -\frac{C_6}{R_{12}^6} \quad (\text{E2})$$

$$C_6 = \frac{2}{3} \frac{r_{SP}^2(Cs)r_{SP}^2(Ar)}{E_{SP}(Cs) + E_{SP}(Ar)}$$

with $r_{SP}(Cs) = \langle 1||r(1)||0\rangle$ and $r_{SP}(Ar) = \langle 1||r(2)||0\rangle$

For the third order calculation, the results we just derived, in section E 2 a, indicate that, in the sum of Eq. (E1), one numerator becomes

$$E = -\frac{\sqrt{6}}{R_{12}^3} \frac{\sqrt{6}}{R_{13}^3} \frac{\sqrt{6}}{R_{23}^3} \frac{\langle 1||r(1)||0\rangle^2}{3} \frac{\langle 1||r(2)||0\rangle^2}{3} \frac{\langle 1||r(3)||0\rangle^2}{3} \times$$

$$\sum_{q_1, q_2, q'_1, q'_2, q_3, q'_3} (-1)^{q_1+q_2+q_3} \delta_{q_1,-q'_1} \delta_{q_2,-q'_2} \delta_{q_3,-q'_3} \times$$

$$\sum_{M, M', M''} (-1)^{M+M'+M''} C_{-M}(\mathbf{e}_{12}) C_{-M'}(\mathbf{e}_{13}) C_{-M''}(\mathbf{e}_{23}) C_{1q_1 1q_2}^{2M} C_{1q'_1 1q_3}^{2M'} C_{1q'_2 1q'_3}^{2M''}$$

but using (8.4(10) and 8.7(15) from [137]) we have

$$\sum_{q_1, q_2, q_3} (-1)^{q_1+q_2+q_3} C_{1q_1 1q_2}^{2M} C_{1-q_1 1q_3}^{2M'} C_{1-q_2 1-q_3}^{2M''} =$$

$$-(-1)^{-M''} 5 C_{2M 2M'}^{2-M''} \begin{Bmatrix} 1 & 1 & 2 \\ 2 & 2 & 1 \end{Bmatrix} =$$

$$-(-1)^{-M''} C_{2M 2M'}^{2-M''} \sqrt{7/12}. \text{ So}$$

$$E = \frac{\sqrt{14}}{9} \frac{\langle 1||r(1)||0\rangle^2}{R_{12}^3} \frac{\langle 1||r(2)||0\rangle^2}{R_{13}^3} \frac{\langle 1||r(3)||0\rangle^2}{R_{23}^3} \times$$

$$\sum_{M, M', M''} (-1)^{M+M'} C_{-M}(\mathbf{e}_{12}) C_{-M'}(\mathbf{e}_{13}) C_{-M''}(\mathbf{e}_{23}) C_{2M 2M'}^{2-M''}$$

and finally using z axis along \mathbf{e}_{12} (so $M=0$ in the previous sum) and θ_i being the inner angles of the 123 triangle with $\cos \theta_1 = \mathbf{e}_{12} \cdot \mathbf{e}_{13}$ and $\cos(\pi - \theta_2) = \mathbf{e}_{12} \cdot \mathbf{e}_{23}$. We get

$$E = \frac{\langle 1||r(1)||0\rangle^2 \langle 1||r(2)||0\rangle^2 \langle 1||r(3)||0\rangle^2}{36 R_{12}^3 R_{13}^3 R_{23}^3} \times$$

$$(1 - 3(\cos(2\theta_1) + \cos(2\theta_2) + \cos(2\theta_3)))$$

So when summing the 6 terms, this finally leads to

$$E_{123}^{(3)} = \frac{4 \langle 1||r(1)||0\rangle^2 \langle 1||r(2)||0\rangle^2 \langle 1||r(3)||0\rangle^2}{36 R_{12}^3 R_{13}^3 R_{23}^3} \times$$

$$(1 - 3(\cos(2\theta_1) + \cos(2\theta_2) + \cos(2\theta_3))) \times$$

$$\frac{\Delta(1) + \Delta(2) + \Delta(3)}{(\Delta(1) + \Delta(2))(\Delta(2) + \Delta(3))(\Delta(1) + \Delta(3))}$$

So in summary

$$E_{123}^{(3)} = \frac{C_9}{R_{12}^3 R_{23}^3 R_{31}^3} \frac{1 - 3(\cos(2\theta_1) + \cos(2\theta_2) + \cos(2\theta_3))}{4} \quad (\text{E3})$$

$$C_9 = \frac{4}{9} r_{SP}^2(Cs) r_{SP}^4(Ar) \frac{E_{SP}(Cs) + 2E_{SP}(Ar)}{2(E_{SP}(Cs) + E_{SP}(Ar))^2 E_{SP}(Ar)}$$

We wrote the C_9 coefficient such that we can restore the historical (Axilrod-Tenner-Mutô [155, 156] form using $1 - 3(\cos(2\theta_1) + \cos(2\theta_2) + \cos(2\theta_3)) = 4(1 + 3\cos(\theta_1)\cos(\theta_2)\cos(\theta_3))$.

These calculations are technical but similar in a way to the case of two atoms under the effect of a static external electric field [157], the physical picture of the dipole of one atom (1 for instance) interacting with the vector electric fields produced by the other dipoles (2) and (3) helps to understand that the final result depends on the angles and distance between atoms.

c. Interaction with Cs in an excited state $|l=1 m\rangle$

To our knowledge, no general simple formula has been derived for the dipole-dipole-dipole interaction with one atom in the excited state (see however Ref. [158] and reference therein). We derive one formula here. For this, we start by the fact that in this case, $|0_1\rangle = |l=1 m\rangle$ and $|m_1\rangle = |l=0 m=0\rangle$. So

$$\sum_{m_1} \langle 0_1|r_{q_1}(1)|m_1\rangle \dots \langle m_1|r_{q'_1}(1)|0_1\rangle =$$

$$\langle 1m|r_{q_1}(1)|00\rangle \dots \langle 00|r_{q'_1}(1)|1m\rangle =$$

$$-C_{1m 1q'_1}^{00} \frac{C_{00 0 1 q_1}^{1m}}{\sqrt{3}} \langle 1||r(1)||0\rangle^2 =$$

$$\delta_{mq_1} \delta_{q_1,-q'_1} (-1)^{q_1} \frac{\langle 1||r(1)||0\rangle^2}{3}$$

The second order leads to $C_6^* = \frac{2}{3} \frac{\langle 1||r(1)||0\rangle^2 \langle 1||r(2)||0\rangle^2}{\Delta(1) + \Delta(2)}$ with

$$E_{12}^{(2)} = -\frac{2C_6^*(\Pi)}{3R_{12}^6} = -\frac{C_6^*(\Pi)}{R_{12}^6} \text{ for } m=0 \quad (\text{E4})$$

$$E_{12}^{(2)} = -\frac{C_6^*(\Sigma)}{6R_{12}^6} = -\frac{C_6^*(\Sigma)}{R_{12}^6} \text{ for } m=\pm 1$$

$$C_6^* = \frac{2}{3} \frac{r_{SP}^2(Cs)r_{SP}^2(Ar)}{E_{SP}(Ar) - E_{SP}(Cs)}$$

so as expected $C_6^*(\Sigma) + 2C_6^*(\Pi) = C_6^*$.

For the third order, we have for a given numerator term:

$$E = -\frac{\sqrt{6}}{R_{12}^3} \frac{\sqrt{6}}{R_{13}^3} \frac{\sqrt{6}}{R_{23}^3} \frac{\langle 1||r(1)||0\rangle^2}{3} \frac{\langle 1||r(2)||0\rangle^2}{3} \frac{\langle 1||r(3)||0\rangle^2}{3} \times$$

$$\sum_{q_1, q_2, q'_1, q'_2, q_3, q'_3} \delta_{mq_1} \delta_{q_1,-q'_1} (-1)^{q_1+q_2+q_3} \delta_{q_2,-q'_2} \delta_{q_3,-q'_3} \times$$

$$\sum_{M, M', M''} (-1)^{M+M'+M''} C_{-M}(\mathbf{e}_{12}) C_{-M'}(\mathbf{e}_{13}) C_{-M''}(\mathbf{e}_{23}) \times$$

$$C_{1q_1 1q_2}^{2M} C_{1q'_1 1q_3}^{2M'} C_{1q'_2 1q'_3}^{2M''}$$

but using z axis along \mathbf{e}_{12} (so $M = 0$) we have

$$E = -\sqrt{\frac{8}{27}} \frac{\langle 1|r(1)|0\rangle^2 \langle 1|r(2)|0\rangle^2 \langle 1|r(3)|0\rangle^2}{R_{12}^3 R_{13}^3 R_{23}^3} \times \sum_{M', M''} (-1)^{M'+M''} C_0(\mathbf{e}_{12}) C_{-M'}(\mathbf{e}_{13}) C_{-M''}(\mathbf{e}_{23}) \times C_{1m1-m}^{20} \sum_{q_3} (-1)^{q_3} C_{1-m1q_3}^{2M'} C_{1m1-q_3}^{2M''}$$

So, $E = \frac{\langle 1|r(1)|0\rangle^2 \langle 1|r(2)|0\rangle^2 \langle 1|r(3)|0\rangle^2}{54R_{12}^3 R_{13}^3 R_{23}^3} f(\theta_1, \theta_2, \theta_3, m)$
with

$$f(\theta_1, \theta_2, \theta_3, m) = -(1 + 3 \cos(2\theta_1) + 3 \cos(2\theta_2) + 9 \cos(2\theta_3)) \quad \text{for } m = 0 \quad (\text{E5})$$

$$f(\theta_1, \theta_2, \theta_3, m) = (5 - 3 \cos(2\theta_1) - 3 \cos(2\theta_2) + 9 \cos(2\theta_3))/4 \quad \text{for } m = \pm 1 \quad (\text{E6})$$

Then, summing the 6 terms (see [154]) finally leads to

$$E_{123}^{(3)} = \frac{2 \langle 1|r(1)|0\rangle^2 \langle 1|r(2)|0\rangle^2 \langle 1|r(3)|0\rangle^2}{27R_{12}^3 R_{13}^3 R_{23}^3} \times f(\theta_1, \theta_2, \theta_3, m) \times \frac{\Delta(1) + \Delta(2) + \Delta(3)}{(\Delta(1) + \Delta(2))(\Delta(2) + \Delta(3))(\Delta(1) + \Delta(3))}$$

so,

$$E_{123}^{(3)} = \frac{C_9^*}{R_{12}^3 R_{13}^3 R_{23}^3} \frac{f(\theta_1, \theta_2, \theta_3, m)}{6} \quad (\text{E7})$$

$$C_9^* = \frac{4}{9} r_{SP}^2(Cs) r_{SP}^4(Ar) \frac{2E_{SP}(Ar) - E_{SP}(Cs)}{2(E_{SP}(Ar) - E_{SP}(Cs))^2 E_{SP}(Ar)}$$

3. Mean field effect and effective two-body potentials

The most accurate way to include this third-order correction for the energy of atoms A is to sum over all B,C pairs of atoms. But due to the lack of information on the short-range part and due to the crude (two-level) estimation made up to now, we can simplify the problem more and use the mean-field approach done in Ref. [75] (see also [74, 159]) by creating a mean-field potential $\bar{E}_{AB}^{(3)} = \sum_C E_{ABC}^{(3)}$ such that the full crystal energy $\frac{1}{2} \left(\sum_{AB} E_{AB}^{(2)} + \frac{1}{3} \sum_{ABC} E_{ABC}^{(3)} \right)$ can be written as sum of two body terms $E_{AB}^{\text{eff}} = (E_{AB}^{(2)} + \frac{1}{3} \bar{E}_{AB}^{(3)})$.

We can thus stay at a two-body level simply by modifying the two-body interaction between atoms by adding $\frac{1}{3} \bar{E}_{AB}^{(3)}$ to the $E_{AB}^{(2)}$ potential interaction curves we already have. This mean-field approach has been proven to be quite accurate for pure crystals, as shown by the so-called Marcelli-Wang-Sadus potential [74, 78, 159–162] and as we demonstrate in Fig. 3 in the Ar-Ar case.

a. Mean field homogeneous assumption

Strangely enough, almost no mathematical derivation of the mean field approach exists though it has been performed as back as in the original paper by Mutô [156] (whose journal reference is almost always wrong) and by Stenschke[75]. Following these works, we replace the sum $\bar{E}_{AB}^{(3)} = \sum_C E_{ABC}^{(3)}$ by an integral assuming Ar atoms uniformly distributed with density $\rho = N/V$ (for solid argon the density $\rho = 280 \text{ a}_0^{-3}$ where a_0 is the Bohr radius). We thus sum over the C atoms (the number 3 above); that is, we average the potential $V = \sum_j E_{12j}^{(3)}$ as $\bar{V} = \rho \int V r^2 \sin \theta dr d\theta d\varphi = 2\pi\rho \int V r^2 \sin \theta dr d\theta$ in spherical coordinate with $\theta = \theta_1$ and $r = R = R_{12}$. We found simpler to use $r_1 = R_{13}, r_2 = R_{23}$ coordinates, as in Ref. [75], such that $\bar{V} = 2\pi\rho \int V \frac{r_1 r_2}{R} dr_1 dr_2$, with an exclusion sphere of radius σ around the atoms A=1 and B=2. Equations (E3) and (E7) lead to

$$\bar{E}_{12}^{(3)} = 2\pi\rho \frac{C_9}{R^6} \frac{4}{3} \quad (\text{E8})$$

$$\bar{E}_{12}^{*(3)} = 2\pi\rho \frac{C_9^*}{R^6} \frac{4}{9} (4 - 3 \log[(R^2 - \sigma^2)/\sigma^2]) \quad \text{for } m = 0$$

$$\bar{E}_{12}^{\pm(3)} = 2\pi\rho \frac{C_9^*}{R^6} \frac{2}{9} (-1 + 3 \log[(R^2 - \sigma^2)/\sigma^2]) \quad \text{for } m = \pm 1$$

Thus, only when the state is isotropic, like the S ground state or equally by summing $m = -1, 0, 1$ for the P state, does the triple dipole interaction not depend on σ .

b. Effective potentials

All results are summarized by Eqs (E2-E8) from where we can extract the effective potentials for the internuclear distance R :

$$E_{AB}^{\text{eff}}(R) = E_{AB}^{(2)}(R) \left(1 - \frac{8\pi\rho C_9}{9 C_6} \right) \quad (\text{E9})$$

$$E_{AB}^{*,\text{eff}}(\Sigma) = E_{AB}^{(2)}(\Sigma) \left(1 - \frac{4\pi\rho C_9^*}{9 C_6^*} (4 - 3 \log[(R^2 - \sigma^2)/\sigma^2]) \right)$$

$$E_{AB}^{\pm,\text{eff}}(\Pi) = E_{AB}^{(2)}(\Pi) \left(1 - \frac{8\pi\rho C_9^*}{9 C_6^*} (-1 + 3 \log[(R^2 - \sigma^2)/\sigma^2]) \right)$$

This form, derived from the long-range triple dipole interaction, can however naturally be extended to the full range of the potential by simply keeping the same formula for all R . The only requirement is the choice of the cut-off because $R > 2\sigma$. Because the short-range part of the potential is clearly not a dipole-dipole one, we smoothly reduce the C_9^* part for $R < 2\sigma$ by multiplying it in Eq. (E9), for all R , by a fortuitous sharp cut-off function $1 - e^{-(R/2\sigma)^{10}}$. A reasonable value for σ might be the nearest neighbor distance in the fcc crystal or the lattice size or the first nearest neighbor Cs-Ar atoms in a given trapping site (see Fig. 6). This may depend on the chosen trapping site to be studied. Another, in principle independent, cut-off should be of the order of the LeRoy

radius that corresponds to the change in the multipole expansion at small R so when the theoretical curves are too different from the long-range part, we used to derive the formula [163, 164]. From all this, we found that a reasonable value can be $\sigma \sim 8a_0$. However, all these parameters (cut-offs and the power 10 in the sharp function) are arbitrary choices that can be optimized. We have modified them a bit (factor 2 typically) to produce the uncertainty in the line position shown in Fig. 5.

c. Approximate calculation of C_6 and C_9 coefficients

Our previous formulae for second Eq. (E2) and (E4), and third-order perturbations Eq. (E3) and (E7), contain the van der Waals interaction coefficients C_6, C_6^*, C_9, C_9^* that we now need to evaluate. For this, we will use an effective two-level approximation, known to be 25% accurate for ground state interactions between rare-gas and alkali atoms [73, 165], and that we are going to use also for the excited states. We will also compare the value found by fitting them to the long-range part of our potential curves to existing results to assess the method's accuracy.

For now on, we will use atomic units for this calculation.

The C_6 coefficient for Ar-Ar found by fitting the theoretical Ar-Ar potential curve by $-C_6/R^6$ is 67, and 380 for Ar-Cs. Eq. (E2) and using the well-known experimental values, $E_{SP}(Cs) \approx 0.0524$ and $E_{SP}(Ar) \approx 0.43$ for the first excited P levels, leads to $r_{SP}(Cs) = 5.4$ and $r_{SP}(Ar) = 3.0$.

These values are acceptable because they are reasonable for the C_6 Cs-Cs coefficient of 5500 (compare to the real value of nearly 6700 [166]) and $C_9(Ar - Ar - Ar) \approx 650$ compared to 525 in Refs. [165, 167] and $C_9(Cs - Cs - Cs) \approx 1500000$ compared to $C_9(Cs - Cs - Cs) \approx 2200000$ in Ref. [73]. However, these values for $r_{SP}(Cs), r_{SP}(Ar), E_{SP}(Cs)$ and $E_{SP}(Ar)$ lead to quite wrong values for the excited Cs*-Ar coefficient of $C_6^*(\Pi) = \frac{2}{3}C_6^* = 310$ compared to 600 in our potential curves and $\frac{1}{6}C_6^* = 80$ compared to 270. Unfortunately, it is not possible to solve this discrepancy for all excited states at once simply because Eq. (E4) gives a ratio 4 between $C_6^*(\Pi)$ and $C_6^*(\Sigma)$ while in our case, the theoretical potential curves give only a factor ~ 2 . This factor 2 is indeed found in many other cases [168, 169].

This discrepancy probably comes from the fact that we have neglected other excited states (like Cs(7s)) that are quite near the Cs excited (6p) level. But, because our purpose is to simulate the Cs spectrum in argon, we will focus more on the Cs-Ar and Cs*-Ar interaction curves than on the Ar-Ar one in order to try to reduce the discrepancy. For this, we choose an intermediate strategy and let free the dipole transitions $r_{SP}(Cs), r_{SP}(Ar)$ and the energy level $E_{SP}(Ar)$, that becomes effective values. This allows us to better reproduce the long-range part of the theoretical potential curve for Cs-Ar and Cs*-Ar. For this, we start with fitting the theoretical potential curve that leads to $\frac{C_6^*}{C_6} \approx 3$. Then Eq. (E2) and (E4) give $\frac{C_6^*}{C_6} = \frac{E_{SP}(Ar)+E_{SP}(Cs)}{E_{SP}(Ar)-E_{SP}(Cs)}$. This leads to $E_{SP}(Ar) = 2E_{SP}(Cs) = 0.10$. Then, using expression Eq. (E2) for the C_6 coefficient for Ar-Ar (67) and Ar-Cs (380) leads to (in atomic units):

$$E_{SP}(Cs) = 0.052 \quad (E10)$$

$$E_{SP}(Ar) \approx 0.10$$

$$r_{SP}(Cs) \approx 4.4$$

$$r_{SP}(Ar) \approx 2.1$$

$$C_6 \approx 370 \quad (E11)$$

$$C_6^* \approx 1200$$

$$C_9 \approx 9100$$

$$C_9^* \approx 54000$$

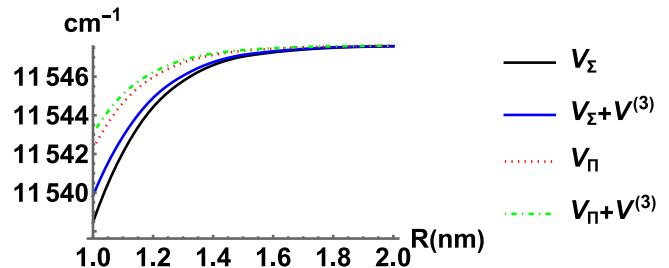


FIG. 10. Cs(6p)-Ar potential curves compared to the one with the effective third-order effect included.

The long-range parts of some potential curves are shown in Fig. 10. These parameters values, and the modification by a factor ~ 2 for the cut-off and the power of the sharp function, have been used in order to produce the uncertainty in the line positions shown in Fig. 5.

- [1] A. Barnes, W. Orville-Thomas, A. Müller, and R. Gaudrès, *Matrix isolation spectroscopy* (Springer Dordrecht, 1981).
- [2] M. Almond and A. Downs, *Spectroscopy of Matrix Isolated Species* (Wiley, Chichester, 1989).
- [3] V. E. Bondybey, A. M. Smith, and J. Agreiter, *Chemical reviews* **96**, 2113 (1996).

- [4] C. Crepin-Gilbert and A. Tramer, *International Reviews in Physical Chemistry* **18**, 485 (1999).
- [5] B. M. Davis, B. Gervais, and J. G. McCaffrey, *The Journal of Chemical Physics* **148**, 124308 (2018).
- [6] G. K. Ozerov, D. S. Bezrukov, and A. A. Buchachenko, *Physical Review B* **103**, 184110 (2021).
- [7] C. Pryor and F. Wilczek, *Physics Letters B* **194**, 137

- (1987).
- [8] M. Arndt, S. Kanorsky, A. Weis, and T. Hänsch, *Physics Letters A* **174**, 298 (1993).
 - [9] M. Kozlov and A. Derevianko, *Physical review letters* **97**, 063001 (2006).
 - [10] A. C. Vutha, M. Horbatsch, and E. A. Hessels, *Atoms* **6** (2018).
 - [11] S. Upadhyay *et al.*, *Physical Review A* **100**, 063419 (2019).
 - [12] C. Braggio *et al.*, *Applied Sciences* **12**, 6492 (2022).
 - [13] D. Budker *et al.*, arXiv preprint arXiv:2203.09488 (2022).
 - [14] M. Safronova *et al.*, *Reviews of Modern Physics* **90**, 025008 (2018).
 - [15] C. Ien, V. Bowers, E. Cochran, and S. Foner, *Physical Review* **126**, 1749 (1962).
 - [16] J. Goldsborough and T. Koehler, *Physical Review* **133**, A135 (1964).
 - [17] W. Weyhmann and F. Pipkin, *Physical Review* **137**, A490 (1965).
 - [18] T. Kanda and T. Ebisu, *Journal of the Physical Society of Japan* **31**, 957 (1971), <https://doi.org/10.1143/JPSJ.31.957>.
 - [19] L. Balling and J. Wright, *The Journal of Chemical Physics* **78**, 592 (1983).
 - [20] J. L. Hollenberg and D. A. Dows, *The Journal of chemical physics* **37**, 1300 (1962).
 - [21] P. Groner, I. Stolkin, and H. H. Gunthard, *Journal of Physics E: Scientific Instruments* **6**, 122 (1973).
 - [22] G. J. Jiang, W. B. Person, and K. G. Brown, *The Journal of Chemical Physics* **62**, 1201 (1975).
 - [23] A. Sinnock and B. Smith, *Physical Review* **181**, 1297 (1969).
 - [24] R. Hahn *et al.*, *Review of Scientific Instruments* **93**, 043302 (2022).
 - [25] D. A. Steck, (2019).
 - [26] S. A. Nepijko, I. Rabin, and W. Schulze, *ChemPhysChem* **6**, 235 (2005).
 - [27] J. D. Patterson and B. C. Bailey, *Solid-state physics: introduction to the theory (third edition)* (Springer Science & Business Media, 2018).
 - [28] B. Smith, *Contemporary Physics* **11**, 125 (1970).
 - [29] J. Venables and B. Smith, (1977).
 - [30] S. Kovalenko and N. Bagrov, *SOVIET PHYSICS SOLID STATE, USSR* **11**, 2207 (1970).
 - [31] J. ShakhsEmampour, R. Pyzalski, M. Vala, and J.-C. Rivoal, *Journal de Physique* **45**, 953 (1984).
 - [32] R. Rudman, *Acta Crystallographica Section A: Crystal Physics, Diffraction, Theoretical and General Crystallography* **34**, 639 (1978).
 - [33] K. Song and R. T. Williams, (2013).
 - [34] W. Schulze and D. Kolb, *Journal of the Chemistry Society, Faraday Transactions 2* **70**, 1098 (1974).
 - [35] G. L. Pollack, *Reviews of Modern Physics* **36**, 748 (1964).
 - [36] Y. K. Tovbin, S. Titov, and V. Komarov, *Physics of the Solid State* **57**, 360 (2015).
 - [37] Y. K. Tovbin, V. Komarov, and E. Gvozdeva, *Protection of Metals and Physical Chemistry of Surfaces* **53**, 591 (2017).
 - [38] N. Tishchenko, *Physica Status Solidi. A, Applied Research* **73**, 279 (1982).
 - [39] N. Tishchenko, *physica status solidi (a)* **83**, 513 (1984).
 - [40] I. V. Leibin, I. S. Kalinina, D. S. Bezrukov, and A. A. Buchachenko, *The Journal of Chemical Physics* **154**, 044305 (2021).
 - [41] L. Blank, D. E. Weeks, and G. S. Kedziora, *The Journal of Chemical Physics* **136**, 124315 (2012).
 - [42] T. Kobayashi, K. Yuki, and L. Matsuoka, *Chemistry Letters* **45**, 1400 (2016).
 - [43] A. A. Medvedev, V. V. Meshkov, A. V. Stolyarov, and M. C. Heaven, *Physical Chemistry Chemical Physics* **20**, 25974 (2018).
 - [44] G. K. Ozerov, D. S. Bezrukov, and A. A. Buchachenko, *Low Temperature Physics* **45**, 301 (2019).
 - [45] N. N. Kleshchina, I. S. Kalinina, I. V. Leibin, D. S. Bezrukov, and A. A. Buchachenko, *The Journal of Chemical Physics* **151**, 121104 (2019).
 - [46] U. K. Deiters and R. J. Sadus, *The Journal of Chemical Physics* **150**, 134504 (2019).
 - [47] V. F. Lotrich and K. Szalewicz, *Physical review letters* **79**, 1301 (1997).
 - [48] P. Schwerdtfeger, R. Tonner, G. E. Moyano, and E. Pahl, *Angewandte Chemie International Edition* **55**, 12200 (2016).
 - [49] D. Bezrukov, N. Kleshchina, I. Kalinina, and A. Buchachenko, *Russian Journal of Physical Chemistry A* **93**, 1505 (2019).
 - [50] M. Lara-Moreno, J. Alvarez-Hernández, H. Negrín-Yuvero, J. G. McCaffrey, and G. Rojas-Lorenzo, *Low Temperature Physics* **45**, 697 (2019).
 - [51] N. N. Kleshchina, K. A. Korchagina, D. S. Bezrukov, and A. A. Buchachenko, *The Journal of Physical Chemistry A* **121**, 2429 (2017).
 - [52] L.-G. Tao *et al.*, *The Journal of Chemical Physics* **143**, 174306 (2015).
 - [53] N. Lam, N. Doan, and L. Dagens, *Journal of Physics F: Metal Physics* **15**, 799 (1985).
 - [54] N. Lam and L. Dagens, *Journal of Physics F: Metal Physics* **16**, 1373 (1986).
 - [55] M. Sabochick, S. Yip, and N. Lam, *Journal of Physics F: Metal Physics* **18**, 349 (1988).
 - [56] H. Zenia, K. Lounis, E. Megchiche, and C. Mijoule, *Computational Materials Science* **124**, 428 (2016).
 - [57] K. Lounis, H. Zenia, E. Megchiche, and C. Mijoule, *Computational Materials Science* **118**, 279 (2016).
 - [58] R. Cotterill and M. Doyama, *Calculation of the Properties of Vacancies and Interstitials: Proceedings* **13**, 47 (1966).
 - [59] A. Damask, *Science* **162**, 448 (1968).
 - [60] R. Johnson, *Journal of Physics F: Metal Physics* **3**, 295 (1973).
 - [61] L. Y. Nemirovich-Danchenko, A. Lipnitskiui, and S. Kul'kova, *Physics of the Solid State* **49**, 1079 (2007).
 - [62] H. Wang, D. Rodney, D. Xu, R. Yang, and P. Veysseyre, *Philosophical Magazine* **93**, 186 (2013).
 - [63] J. Peng, S. Bahl, A. Shyam, J. A. Haynes, and D. Shin, *Acta Materialia* **196**, 747 (2020).
 - [64] S. Ruder, arXiv preprint arXiv:1609.04747 (2016).
 - [65] S. H. Haji and A. M. Abdulazeez, *PalArch's Journal of Archaeology of Egypt/Egyptology* **18**, 2715 (2021).
 - [66] D. P. Kingma and J. Ba, arXiv preprint arXiv:1412.6980, Published as a conference paper at the 3rd International Conference for Learning Representations, San Diego, 2015 (2014).
 - [67] T. Dozat, (2016).
 - [68] J. Simons, *An introduction to theoretical chemistry* (Cambridge University Press, 2003).

- [69] M. Heaven and A. Stoliarov, Potential energy curves for alkali metal-rare gas exciplex lasers, in *41st Plasma-dynamics and Lasers Conference*, p. 4877, 2010.
- [70] M. Ryan, M. Collier, P. d. Pujó, C. Crépin, and J. G. McCaffrey, *The Journal of Physical Chemistry A* **114**, 3011 (2010).
- [71] E. Jacquet, D. Zanuttini, J. Douady, E. Giglio, and B. Gervais, *The Journal of chemical physics* **135**, 174503 (2011).
- [72] P. Moroshkin, A. Hofer, and A. Weis, *Physics reports* **469**, 1 (2008).
- [73] M. Diaz Peña, C. Pando, and J. Renuncio, *The Journal of Chemical Physics* **73**, 1750 (1980).
- [74] S. Dridi, M. B. Amar, M. Abderraba, and J.-P. Passarello, *Fluid Phase Equilibria* **562**, 113563 (2022).
- [75] H. Stenschke, *The Journal of chemical physics* **100**, 4704 (1994).
- [76] B. Akhouri and J. Solana, *Physica A: Statistical Mechanics and its Applications*, 128280 (2022).
- [77] H. Berendsen, *Simulating the physical world* (Cambridge University Press Cambridge, 2007).
- [78] P. Ströker, R. Hellmann, and K. Meier, *Physical Review E* **105**, 064129 (2022).
- [79] M. Lax, *The Journal of chemical physics* **20**, 1752 (1952).
- [80] E. J. Heller, *The Journal of Chemical Physics* **68**, 2066 (1978).
- [81] R. S. Mulliken, *The Journal of Chemical Physics* **55**, 309 (1971).
- [82] J. Tellinghuisen, The franck-condon principle, in *Photons and Continuum States of Atoms and Molecules: Proceedings of a Workshop Cortona, Italy, June 16–20, 1986*, pp. 149–156, Springer, 1987.
- [83] L. Barragán-Gil and R. Walser, *American Journal of Physics* **86**, 22 (2018).
- [84] J. P. Bergsma, P. H. Berens, K. R. Wilson, D. R. Fredkin, and E. J. Heller, *The Journal of Physical Chemistry* **88**, 612 (1984).
- [85] J. A. Boatz and M. E. Fajardo, *The Journal of chemical physics* **101**, 3472 (1994).
- [86] E. Pavarini, *Correlated electrons: from models to materials* **2**, 6 (2012).
- [87] B. S. Tsukerblat, *Group theory in chemistry and spectroscopy: a simple guide to advanced usage* (Courier Corporation, 2006).
- [88] M. S. Dresselhaus, G. Dresselhaus, and A. Jorio, *Group theory: application to the physics of condensed matter* (Springer Science & Business Media, 2007).
- [89] W. Hergert and R. M. Geilhufe, *Group Theory in Solid State Physics and Photonics: Problem Solving with Mathematica* (Wiley-VCH, 2018), ISBN: 978-3-527-41133-7.
- [90] J. Van Vleck, *The Journal of Chemical Physics* **7**, 72 (1939).
- [91] Y. Toyozawa and M. Inoue, *Journal of the Physical Society of Japan* **21**, 1663 (1966).
- [92] K. Cho, *Journal of the Physical Society of Japan* **25**, 1372 (1968).
- [93] M. Sturge, The jahn-teller effect in solids, in *The Jahn-Teller Effect in Solids*, edited by F. Seitz, D. Turnbull, and H. Ehrenreich, , *Solid State Physics Vol. 20*, pp. 91–211, Academic Press, 1968.
- [94] P. Lund, D. Smith, S. Jacobs, and P. Schatz, *The Journal of Physical Chemistry* **88**, 31 (1984).
- [95] J. Ammeter and D. Schlosnagle, *The Journal of Chemical Physics* **59**, 4784 (1973).
- [96] I. Bersuker, *Coordination Chemistry Reviews* **14**, 357 (1975).
- [97] F. Forstmann, D. Kolb, D. Leutloff, and W. Schulze, *The Journal of Chemical Physics* **66**, 2806 (1977).
- [98] D. Kolb, D. Leutloff, W. Schulze, and F. Forstmann, *Berichte der Bunsengesellschaft für physikalische Chemie* **82**, 33 (1978).
- [99] M. O’Brien, *Journal of Physics C: Solid State Physics* **4**, 2524 (1971).
- [100] H.-J. Stöckmann, *Zeitschrift für Physik B Condensed Matter* **54**, 229 (1984).
- [101] I. Bersuker, *The Jahn-Teller effect and vibronic interactions in modern chemistry* (Springer Science & Business Media, 2013).
- [102] M. Jakob, H. Micklitz, and K. Luchner, *Physics Letters A* **57**, 67 (1976).
- [103] M. Jakob, H. Micklitz, and K. Luchner, *Physics Letters A* **61**, 265 (1977).
- [104] K. Luchner and H. Micklitz, *Journal of Luminescence* **18**, 882 (1979).
- [105] R. Lambo *et al.*, *The Journal of chemical physics* **137**, 204315 (2012).
- [106] R. Lambo *et al.*, *Physical Review A* **104**, 062809 (2021).
- [107] M. Wagner, *The Journal of Chemical Physics* **41**, 3939 (1964).
- [108] T. H. Keil, *Physical Review* **140**, A601 (1965).
- [109] X. Shi-Jie, *Acta Phys. Sin* **68** (2019).
- [110] Y. Zhang, *Journal of Semiconductors* **40**, 091102 (2019).
- [111] C. A. Bates, *Physics reports* **35**, 187 (1978).
- [112] C. Bates, J. Dunn, and E. Sigmund, *Journal of Physics C: Solid State Physics* **20**, 1965 (1987).
- [113] I. Bersuker, *The Jahn-Teller* (Cambridge University Press, New York, 2006).
- [114] M. O’Brien and S. Evangelou, *Journal of Physics C: Solid State Physics* **13**, 611 (1980).
- [115] J. Rose, D. Smith, B. Williamson, P. Schatz, and M. O’Brien, *The Journal of Physical Chemistry* **90**, 2608 (1986).
- [116] B. Hüpper and B. Eckhardt, *Physical Review A* **57**, 1536 (1998).
- [117] E. Wigner, *Physical Review* **40**, 749 (1932).
- [118] E. J. Heller, *The Journal of Chemical Physics* **65**, 1289 (1976).
- [119] J. Shao, J.-L. Liao, and E. Pollak, *The Journal of chemical physics* **108**, 9711 (1998).
- [120] Y. Japha and B. Segev, *Physical Review A* **65**, 063411 (2002).
- [121] B. Segev, *Journal of Optics B: Quantum and Semiclassical Optics* **5**, S381 (2003).
- [122] A. Sergeev and B. Segev, *The Journal of chemical physics* **118**, 5852 (2003).
- [123] E. Pollak and J. Cao, *Physical Review A* **107**, 022203 (2023).
- [124] O. Anatole von Lilienfeld and A. Tkatchenko, *The Journal of chemical physics* **132**, 234109 (2010).
- [125] M. Gross and F. Spiegelmann, *The European Physical Journal D-Atomic, Molecular, Optical and Plasma Physics* **4**, 219 (1998).
- [126] J. D. Hewitt *et al.*, *The Journal of Physical Chemistry A* (2023).
- [127] R. A. Corbin and M. E. Fajardo, *The Journal of chemical physics* **101**, 2678 (1994).

- [128] S. L. Laursen and H. E. Cartland, *The Journal of chemical physics* **95**, 4751 (1991).
- [129] M. Guarise, *The European Physical Journal Plus* **137**, 1 (2022).
- [130] R. Lambo *et al.*, arXiv preprint arXiv:2212.09232 (2022).
- [131] G. Koyanagi *et al.*, arXiv preprint arXiv:2211.14804 (2022).
- [132] R. M. Geilhufe and W. Hergert, *Frontiers in Physics* **6**, 86 (2018).
- [133] A. Devonshire, *Proceedings of the Royal Society of London. Series A-Mathematical and Physical Sciences* **153**, 601 (1936).
- [134] S. K. Misra, *Multifrequency Electron Paramagnetic Resonance: Theory and Applications*, 327 (2011).
- [135] I. D. Ryabov, *Applied Magnetic Resonance* **35**, 481 (2009).
- [136] C. D. Lewis and D. E. Weeks, *The Journal of Physical Chemistry A* **121**, 3340 (2017).
- [137] D. Varshalovich, A. Moskalev, and V. Khersonskii, *Quantum theory of angular momentum* (World Scientific, 1988).
- [138] P. P. Man, *Concepts in Magnetic Resonance Part A* **45**, e21385 (2016).
- [139] J. W. Kenney III, J. A. Boatz, and H. A. Terrill Vosbein, *International journal of quantum chemistry* **103**, 854 (2005).
- [140] U. Hergenbahn, *Journal of Physics B: Atomic, Molecular and Optical Physics* **37**, R89 (2004).
- [141] W. Siebrand, *The Journal of Chemical Physics* **46**, 440 (1967).
- [142] K. F. Freed and S. Lin, *Chemical Physics* **11**, 409 (1975).
- [143] S. Mukamel, *The Journal of Chemical Physics* **77**, 173 (1982).
- [144] I. M. Ansari, E. R. Heller, G. Trenins, and J. O. Richardson, *Philosophical Transactions of the Royal Society A* **380**, 20200378 (2022).
- [145] V. Tatarskii, *Soviet Physics Uspekhi* **26**, 311 (1983).
- [146] M. Hillery, R. F. O'Connell, M. O. Scully, and E. P. Wigner, *Physics reports* **106**, 121 (1984).
- [147] W. B. Case, *American Journal of Physics* **76**, 937 (2008).
- [148] D. K. Ferry and M. Nedjalkov, *The Wigner function in science and technology* (IoP Publishing, 2018).
- [149] S. Kallush, B. Segev, A. Sergeev, and E. Heller, *The Journal of Physical Chemistry A* **106**, 6006 (2002).
- [150] B. Segev and A. Sergeev, *Chemical physics letters* **367**, 382 (2003).
- [151] E. R. Heller and J. O. Richardson, *The Journal of Chemical Physics* **152**, 244117 (2020).
- [152] F. Agostini and B. F. Curchod, *Chemistry without the born-oppenheimer approximation*, 2022.
- [153] R. Bell, *Journal of Physics B: Atomic and Molecular Physics* (1968-1987) **3**, 751 (1970).
- [154] Y. Midzuno and T. Kihara, *Journal of the Physical Society of Japan* **11**, 1045 (1956).
- [155] B. Axilrod and E. Teller, *The Journal of Chemical Physics* **11**, 299 (1943).
- [156] Y. Muto, *Nippon Sugaku-Buturigakkwaishi* **17**, 629 (1943).
- [157] M. Lepers and O. Dulieu, *Physical Chemistry Chemical Physics* **13**, 19106 (2011).
- [158] P.-G. Yan, L.-Y. Tang, Z.-C. Yan, and J. F. Babb, *Physical Review A* **104**, 022807 (2021).
- [159] M. H. Muser, S. V. Sukhomlinov, and L. Pastewka, arXiv preprint arXiv:2204.09563 (2022).
- [160] S. Grimme, A. Hansen, J. G. Brandenburg, and C. Banwarth, *Chemical reviews* **116**, 5105 (2016).
- [161] P. Xu, M. Alkan, and M. S. Gordon, *Chemical Reviews* **120**, 12343 (2020).
- [162] U. K. Deiters and R. J. Sadus, *The Journal of Physical Chemistry B* **125**, 8522 (2021).
- [163] R. J. Le Roy, *Canadian Journal of Physics* **52**, 246 (1974).
- [164] J. Kielkopf, *The Journal of Chemical Physics* **61**, 4733 (1974).
- [165] K. Tang, *Physical Review* **177**, 108 (1969).
- [166] T. Gould and T. Bucko, *Journal of chemical theory and computation* **12**, 3603 (2016).
- [167] R. Bell and A. Kingston, *Proceedings of the Physical Society* (1958-1967) **88**, 901 (1966).
- [168] B. Bussery, M. Aubert-Frécon, and M. Saute, *Chemical physics* **109**, 39 (1986).
- [169] J.-Y. Zhang and J. Mitroy, *Physical Review A* **76**, 022705 (2007).